Contens

Chapter 1

Chapter 2

Chapter 3

Chapter 4

Chapter 5

Chapter 6

Chapter 7

Chapter 8

Abstract

This Thesis presents a dissertation about an experimental method, and a subsequent numerical data post processing, having as goal the heat transfer coefficient and adiabatic effectiveness measurement in gas turbine film cooling problems.

The present work has been developed beginning from an aerodynamic characterization of a linear nozzle cascade, cooled at the trailing edge by a *cutback* geometry, mounted in a suction-type wind tunnel present in the University of Bergamo turbomachinery laboratory. In second instance the thermodynamic problem was studied. After a bibliographic analysis, an optimization method based on transient technique has been implemented to process the experimental data, in order to obtain target coefficients.

The second part of the thesis regard a simpler kind of problem. Indeed, in order to test the optimization method, a new series of test were performed, on a flat plate wind tunnel.

Chapter 1

Introduction to film cooling in gas turbines

1.1 Introduction

Talking about turbogas engines, one of the most important parameters is the *Turbine Inlet Temperature* (TIT) which has a direct influence on the mass work produced by the machine and on its efficiency, indeed increasing that temperature, follows an increase of the produced work and efficiency; this phenomenon is hampered by material constrains like melting point and mechanical limits at the high temperature. Usually those materials lose their mechanical properties around 900° C, when *Creeping* phenomena are observed. It is easy to understand the necessity to cool down the exposed parts to the hot flux coming from the combustion chamber (actually, in last generation engines the TIT is about 1500 °C) (fig. 1.1). High turbine performances requested to the modern turbines oblige to adopt complex cooling systems in order to protect the internal engine surfaces. These systems consists in a combination of internal and external convective cooling.

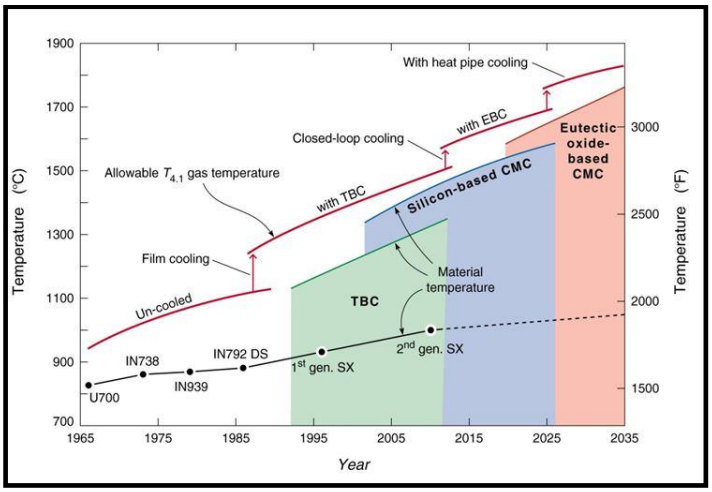

Figure 1.1 : Turbine Inlet Temperature trend

1.2 Cooling Techniques [1.1]

Film cooling consists in drawing a flow of air from the compressor, by-pass the combustion chamber, and inject that cool gas through apposite holes in such a way to cover the engine internal surfaces with a thin cool film (*full coverage method*). Obviously this technique modifies the turbine gas expansion, indeed the two temperature gas mixing modifies the thermodynamic cycle. Follows a comparison between the uncooled and the cooled cycle (fig. 1.2) .

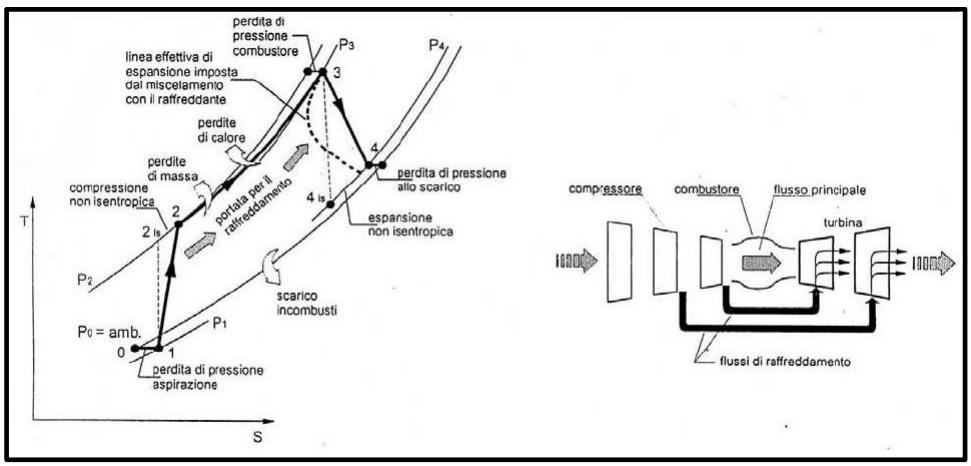

Figure 1.2 : on the left : the real thermodynamic cycle (note the difference between the ideal and the real turbine expansion); on the right : a scheme of the mass flow use.

As previously exposed, there are more than one way to cool down a turbine, here are presented the most used:

a) *Internal convective cooling* : an internal closed cooling circuit is obtained into the interested parts.

b) *Impingement* : it's a variant of the internal cooling used particularly to cool down the most critical points. It consists in a high velocity air jet directed trough the interested point in order to increase the convective coefficient.

c) *Film cooling* : a portion of coolant outflows from holes or slots obtained on the internal surfaces, to cover up these surfaces and hence to protect them from the direct contact with the hot gasses. Due to the mixing phenomena, the efficiency of this technique decreases by increasing the distance from the hole.

d) *Full coverage* : it is the same of the precedent technique, but in this case the holes are distributed over the entire interested surface, so as to better protect it, and increase the exchange surface.

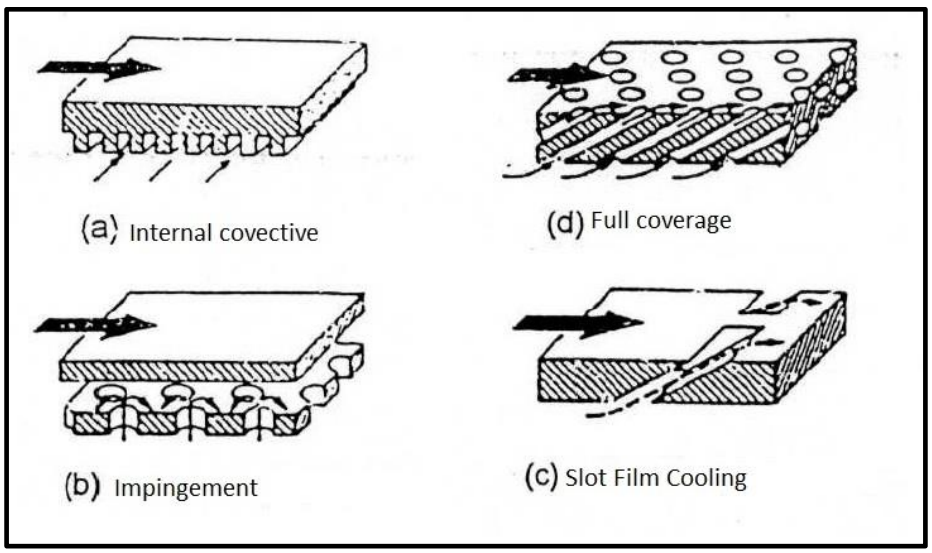

Figure 1.3 : Film cooling systems.

Usually the first four methods described are used together, except the last one which presents some issues due to the fouling of the pores. The main idea is that the first two methods cool the internal surfaces, while the external is cooled by film (fig. 1.4-1.5) .

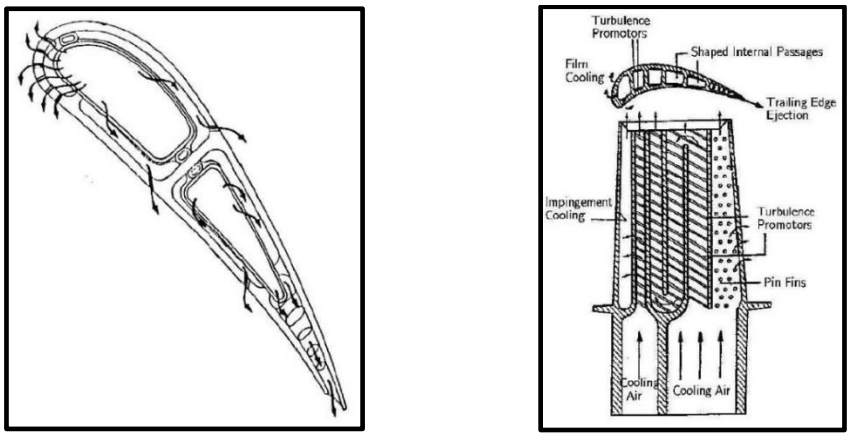

Figure 1.4 : Airfoil cooling systems.

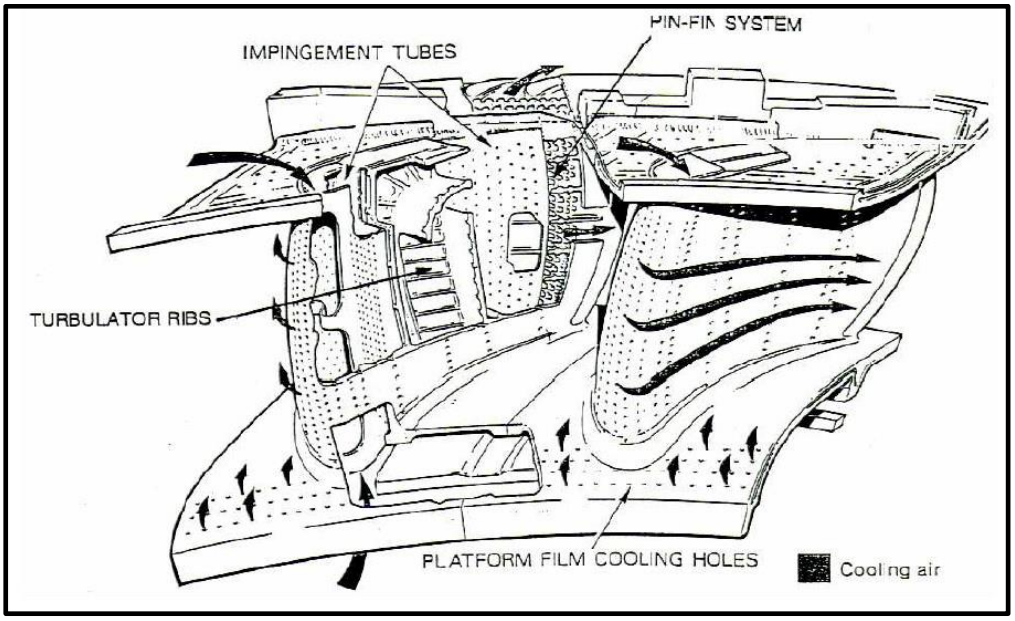

Figure 1.5 : First stage stator cooled section .

1.3 Parameters

Starting from Goldstein film cooling study [1.2], research has been improved by many other studies mostly based on simplified geometries, allowing to focus the attention over groups of parameters that govern the injection conditions (holes geometry, non-dimensional ratios, Turbulence, Reynolds number, boundary layer thickness etc…) .
The most important parameters used to describe the heat transfer performance are the adiabatic Effectiveness (1.1) and the convective heat transfer coefficient (1.2):

$$\eta_{Ad} = \frac{T_{Ad,w} - T_\infty}{T_C - T_\infty} \tag{1.1}$$

$$h = \frac{q_w}{(T_{Ad,w} - T_w)} \tag{1.2}$$

where:

- $T_{Ad,w}$ = is the adiabatic wall temperature;
- T_C = is the coolant temperature;
- T_∞ = is the mainstream temperature;
- T_w = is the wall local temperature;
- q_w = is the heat flux exchanged between wall and fluid.

Both those parameters allow to define the quality of the cooling system, but nothing they suggest about the injection conditions. To describe, reply and compare different test conditions, and in the end to apply to the turbomachinery practical applications, the similitude theory is used. The more frequent non-dimensional parameters used are:

Density Ratio	$\boldsymbol{DR = \frac{\rho_C}{\rho_\infty}}$
Mass Flow Ratio	$\boldsymbol{MFR = \frac{\dot{m}_C}{\dot{m}_\infty}}$
Blowing Ratio	$\boldsymbol{BR = \frac{\rho_C . v_C}{\rho_\infty . v_\infty}}$
Momentum Flux Ratio	$\boldsymbol{I = \frac{\rho_C . v_C^2}{\rho_\infty v_\infty^2}}$
Bleed Flow Rate	$\boldsymbol{BFR = \frac{\dot{m}_C}{\rho_\infty . v_\infty . a_1 . b}}$

Where the subscript "C" means coolant," ∞" means the mainstream and a_1 and b are the height and the width of the admission section.

1.4 Trailing Edge cooling

Blade's trailing edge is one of the most critical parts to be protected, because the cooling system must be able to ensure the material within an acceptable temperature range, while maintaining a limited thickness in order to reduce the aerodynamic losses due to the wake effect. Traditionally this airfoil part is externally cooled by film cooling method, where the injection holes or slots are often arranged with fins and internal turbulator having a double purpose: the first is to modify the fluid dynamic to improve the heat exchange, and in second instance to ensure the mechanical strength. Moreover, often these holes and slots are not made exactly on the trailing edge, but in a retracted position on the pressure side (as later showed) in such a way to cool that face by convection, and the suction side by conduction through the material. This choice has two main motivations:

- Because the last part of the pressure side is subjected to a greater thermal exchange, due to a possible boundary layer transition;
- Because it is better to avoid to work on the suction side, where separation is expected to take place due to the adverse pressure gradient.

1.5 State of the art

In the literature some studies about the trailing edge cooling are documented, from the aerodynamic to the thermal and manufacturing points of view. Most of these works are focused on the influence of the internal channel geometry on the internal convective heat transfer coefficient (e.g. [1.3]), but nothing is said about the possibility to eject that fluid to obtain a film cooling system. Indeed the internal geometry will influence for sure the outlet conditions, the wake structure and the loss generation.

Using a cutback geometry to cool this airfoil section, the injected fluid will cool it by convection and the suction side by thermal conduction. This solution has to ensure high adiabatic effectiveness to be able to refrigerate the pressure side, hence it must have high convective coefficient, in order to guarantee the suction side conditions. Thermal performances has been evaluated downstream the ejection zone of some cutback geometries by using flat plate tests as simplified model [1.3 , 1.4] while discharge characteristics have been studied in a low Mach wind tunnel, by varying the cutback extension [1.5 , 1.6].

Martini et al. [1.7] conducted an experimental and numerical investigation about an airfoil used in a modern gas turbine, housing a cutback preceded by two rows of holes (fig. 1.6) . The lateral ribs spacing is twice their width (and their height), and the cutback height as well, is equal to their width. Seeing that ribs have fillet radii

equal to the half part of the hole height, the coolant jets have circular section and are tangent to the cutback plane.

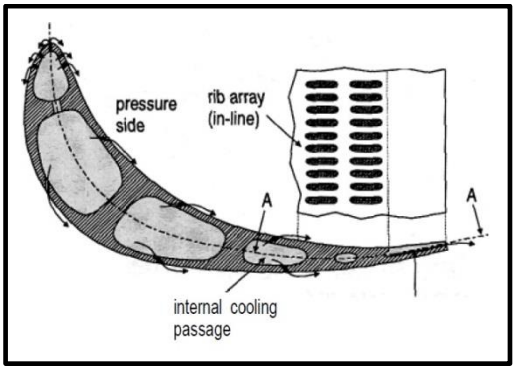

Figure 1.6 : Turbine airfoil section with trailing edge cooled by cutback geometry on the pressure side.

This study is focused on the adiabatic effectiveness downstream the cutback till the trailing edge, and on the pressure distribution between the fins, at different Mass Flow Ratio, and Mach numbers (Ma = 0.35 – 1.1). Adiabatic temperature maps show that coolant has a strong interaction with the main flow, indeed, their tests show that this interaction allows three jets to merge, thus giving a uniform temperature distribution. It is important to note that this cooling configuration results not desirable for that airfoil. Moreover, it seems that the mixing between the two fluxes causes an additional thermal stress to the trailing edge.
Same authors in 2006 [1.8] conducted an experimental study about the cooling performance on different geometric configurations and positions of the same injection slots but related to different cutback geometries. Main results were the following:

- Trailing edge hole's discharge coefficient tends to increase as the coolant Reynolds number increase; obviously a dependency from the internal duct geometries does exist. Anyway, defining a discharge coefficient based on the throat section of the coolant duct, very similar values are obtained for all geometries;
- Cooling efficiency is strongly influenced by the internal slot design, that could origin vortex shedding phenomenon. Numerical studies show that in correspondence of the cutback lip, the flow generates instability vortices, which are the responsible of the fast cooling performance decay through the trailing edge. This phenomenon is known as shear layer vortices. This

hypothesis is confirmed by few numerical and experimental studies, an example is reported in fig. 1.7.

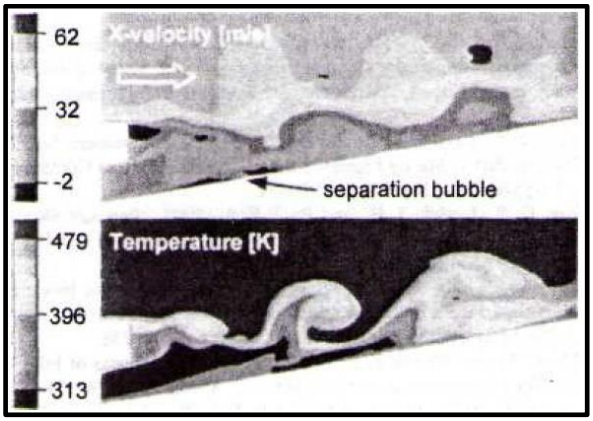

Figure 1.7 : numerical simulation on velocity and temperature field in a transversal section of a cutback geometry. Note the vortex instability that begins from the lip and increase trough the trailing edge.

Heat transfer coefficient downstream the slots shows a rapid increase with respect to the values obtained in a turbulent boundary layer on a flat plate without injection. Tests demonstrate that internal duct design has a heavy influence in the first part of the cutback ($x/H < 5$) while the influence of the Blowing Rate (hence the coolant Reynolds number) extends for the rest of the surface.

Furthermore in the first zone, just attached to the slot exit, heat transfer coefficient has very low values especially in the zone where the flux is not influenced by turbulence generated from the ribs. Probably this behavior is due to a local separation bubble. Moreover, the high acceleration that the coolant has in the convergent section of the internal duct could be the second reason for the low thermal exchange of this surface portion.

In the same period, Ames et al [1.10] demonstrate that a cutback geometry has an important role in the aerodynamic loses generation, proportional to the injected mass flow. Indeed, from experimental data, it has been noted that for Mass Flow Rate lower than the design value, aerodynamic losses tends to increase, while for MFR equal or greater than the design one, the coolant flow gives energy to the mainstream, resulting in a loss reduction.

Similar results were found by Rehder too [1.11] who did aerodynamic and thermodynamic tests on a linear cascade with different trailing edge cooling injection configurations at German Aerospace Center (DLR) in Gottingen.

He has chosen a rotor transonic profile with a very thin trailing edge (fig. 1.8), and tested three different configurations: the first one has a central injection hole, the second one has a cutback on the pressure side with ribs and slots as diffusers, and the last one has only injection holes on the pressure side. In that work data are referred to subsonic and transonic regimes, with MFR lower than 2% . Loss analysis has been done trying to separate the contribution of shock waves, pressure and suction side boundary layers and mixing between main and secondary flow. Measurement techniques used to detect these contribution were Schlieren visualizations for the shock waves, while to obtain the pressure fields, pressure probes have been used. Results show that the central hole solution decreases mixing losses, hence the total losses decreases. Major losses level are introduced by the cylindrical holes configuration, in particular cutback injection geometry reveals huge mixing losses, due to the low secondary flux momentum, which is slowed inside the slots. It is possible to say that the injection velocity has an enormous influence on the cascade losses.
A similar research study was done in the frame of an European research program in 2009 by Dannhauer [1.12]; this project was supposed to investigate the cooling efficiency on the trailing edge pressure side, in a linear cascade wind tunnel (EGG) always in Gottingen DLR, using the same injection geometries described before.

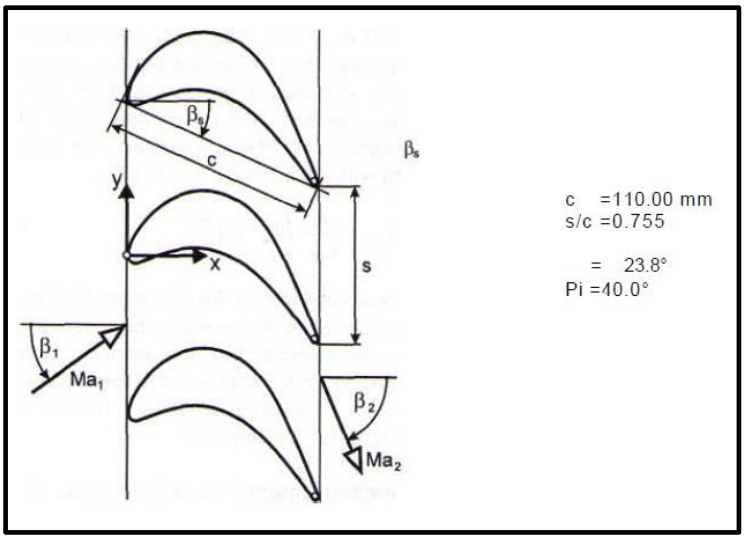

Figure 1.8 : Dannhauer cascade [1.10] .

Two trailing edge cooling geometries were used: the first configuration has a cutback on the pressure side (fig. 1.9), while the second has a cylindrical row of holes on the same airfoil side (fig 1.10).

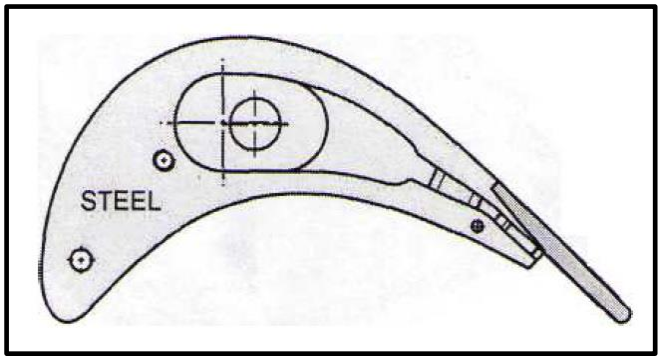

Figure 1.9 : lateral section of the Dannhauer cutback [1.10]

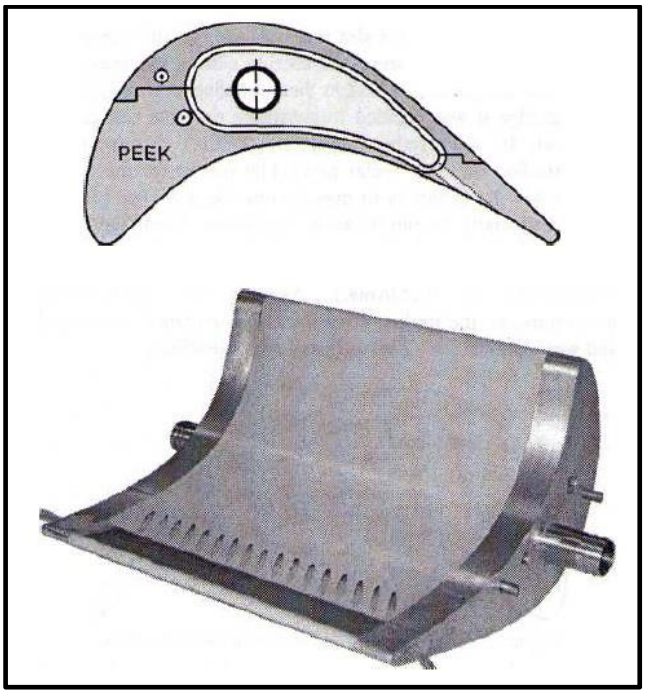

Figure 1.10 : Dannhauer holes cooling geometry [1.10]

Superficial temperature has been detected through a combination of thermocouples and IR thermography. Preliminary studies demonstrate the efficiency of using metallic surfaces, disposed on the other blades, as mirror to the IR thermography. In this way it is possible a better observation of hide surfaces, like the pressure side in a cascade. The IR camera was situated outside the free stream, in order to avoid any influence with the flux, and on every tested geometry were mounted till seven

thermocouples on each side of the trailing edge to allow an in situ IR camera calibration. Results for the cutback configuration shows that for MFR about 0.5% a fluid accumulation is located just before the slot; this is due to a *dead water vortex* in the cutback zone. For MFR equal to 1%, this dead zone begins to be filled by the cold flux, and for greater MFR the efficiency distribution is less homogeneous, due to the coolant separation near some ribs or internal turbulator.

Talking about the holes row cooling configuration, the cooling efficiency increases increasing MFR. Laterally averaged values show that this is the better case, also because this is the geometry with less total losses.

Chapter 2

Linear cascade facility and measurement techniques

2.1 Background

It is clear that film cooling is very important to improve the turbomachinery performances, and its study is hence very important to achieve higher efficiency. It is as much important to acquire as many data as possible about surface's thermal and aerodynamic behavior, in order to clarify the convective coefficient distribution, and the mixing mechanism between mainstream and coolant and to adjust the injection geometries. Despite the computational power has increased in the last years, it remains impossible to compute exactly the interactions between fluids and machines' internal surfaces. It's easy to understand that in addition to the numerical techniques, another instrument is necessary to investigate the cooling performances: *wind tunnels*. In this section the facility used in University of Bergamo laboratory, and the measurement techniques used to assess the aerodynamic behavior of coolant

to mainstream mixing process in a linear gas turbine cascade with cutback trailing edge will be described.

2.2 Linear cascade Wind Tunnel

The linear cascade facility object of this investigation is a low velocity suction type wind tunnel too (fig.2.1).

Figure 2.1 : linear cascade wind tunnel .

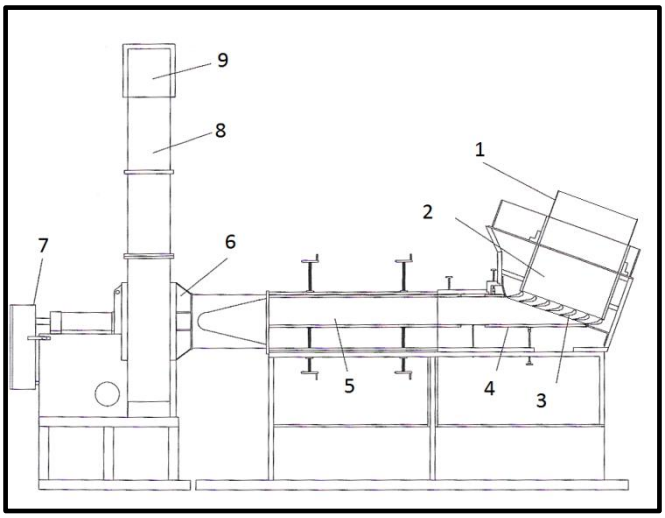

Figure 2.2 : Wind tunnel layout .

In figure 2.2 the facility layout is showed; the following components can be recognized:

1. Filter : necessary to purify the mainstream and hence preserve probes and measurement surfaces;
2. Inlet : it's composed by a convergent duct, to induce a gradual boundary layer growth, and by a straight duct, to obtain a fully developed flux at the end of it.
3. Test Section : here are situated the airfoils and probes;
4. Tailboard : it allows to modify the exit flow in order to obtain a periodical flux at cascade outlet;
5. Diffuser : this section allows to increase the outflow pressure, in order to reduce the pressure ratio over the fan.
6. Centrifugal Fan;
7. Electrical Engine;
8. Outflow diffuser;
9. Outflow.

2.3 Airfoil geometry

The six-blades linear turbine cascade investigated in the present study is shown in Fig. 2.3. The original design of the airfoil, which is typical of a first stage nozzle guide vane of high pressure turbine, was properly scaled down (0.73:1). The vanes have a chord length of 142.1 mm (the axial chord is 68.3 mm) and the pitch is 148.3 mm, which gives a pitch-to-chord ratio of 1.04. The vane height is 98 mm. The aspect ratio is 0.69. Since this value is relatively low, secondary flows are supposed to have a significant effect on aerodynamic performance. The vane profile imposes a design flow turning of 70° with an inlet angle of 90°. The vane is characterized by a Zweifel coefficient of 1.18, indicating a highly loaded vane. The throat is located at X/c_{ax} = 47% along the suction side. All geometrical parameters are summarized in Table 2.1.

All the tests were performed at zero incidence. The cooling design is also reported in figure 2.3.

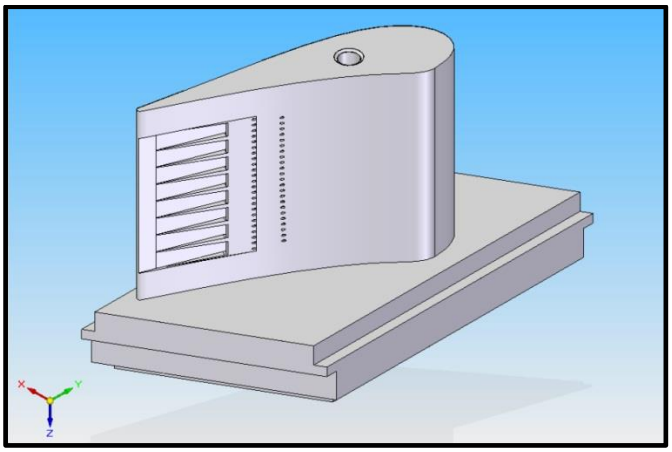

Figure 2.3 : Airfoil and internal cooling system .

Blade number	N	6
Pitch	S	148.33 (mm)
Axial Chord	C_{ax}	68.38 (mm)
Blade's height	H	98 (mm)
Pitch-chord ratio	S/C	1.043894
Aspect Ratio	H/C	0.69

Table 2.1 : Airfoil dimensions and parameters .

Only the three central vanes are cooled over 70% of the whole vane height. The cooling system features two rows of cylindrical holes followed by a cutback slot. The first row has 23 holes at $X/C_{ax} = 0.52$, while the second has 24 holes staggered with respect to the first, situated at $X/C_{ax} = 0.64$. Holes diameter (D) is 1.05 mm and are positioned with a pitch equal to 2.76D, with an injection angle of 30° to the vane surface. The *cutback* is made of 8 equally spaced rectangular slots, 6.75 x 1.43 mm in size, located 40 mm from the trailing edge, separated by fins that are part of the internal turbulator system (fig. 2.4). The span wise rib width is 2 mm. The thickness of the ribs gradually decreases to zero, at a distance of 8 mm from the vane trailing edge. These fins have a double purpose: as turbulence promoters and as structural reinforcement.

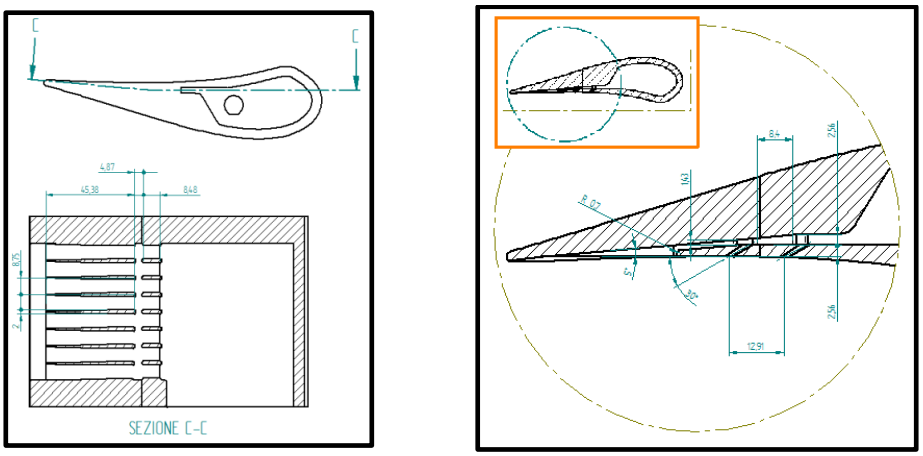

Figure 2.4 : internal turbulator system and cutback .

The cascade's vanes are realized using a 3D printer, except the central one, which has been realized in Plexiglas® (figure 2.5) using a 4 axis CNC. This choice has been done because that material is more homogeneous than the one used for the rapid prototyping, composed by a glued chalk powder.

Figure 2.5 : Plexiglas® blade and internal cooling system .

The coolant air is independently supplied to the three vanes by a 3 kW radial fan. A variable frequency drive regulates the fan speed. After passing through an orifice meter, the coolant enters a plenum chamber. Flexible ducts connect the

plenum chamber to the three vanes cavity. A heater installed inside the plenum allows to rise the coolant temperature up to about 55°C as a maximum.

2.4 Cascade operating conditions

The cascade was tested at a constant exit Mach number M_{2is} of 0.2, corresponding to a Re_{2is} of 6.5 10^5, and at a low Tu_1 of 1.6% (Table 2.2). The low speed operating condition was selected to preserve the mechanical integrity of the optical window required by the IR thermometry application. Cascade operating conditions were controlled through a continuous monitoring of inlet total and static pressure and exit static pressure (31 wall taps located at X/c_{ax} = 145% - Figure 2.6). Inlet total pressure and static pressure were measured in the admission section, about $1.6c_{ax}$ upstream of the cascade inlet plane by a three-hole probe.

Coolant-to-mainstream mass flow rate ratios up to MFR = 2.8%, corresponding to MFR_{slot} = 2.0%, were tested. Injection conditions (Table 2.3) were controlled through a continuous monitoring of the coolant-to-mainstream mass flow ratio MFR and the coolant total pressure and temperature in the three vane feeding chambers. The injected mass flow was measured by an orifice meter.

M_{2is} = 0.2
Re_{2is} = 6.5 10^5
Tu_1 = 1.6 %
δ_1 = 23.6 *mm*
MFR = 1.0 – 2.7 %

Table 2.2. Cascade geometry and operating conditions.

***MFR* (%)**	1.0	1.5	2.0	2.7
$\boldsymbol{MFR_{slot}}$	1.0	1.24	1.52	2.0

Table 2.3. Coolant injection conditions.

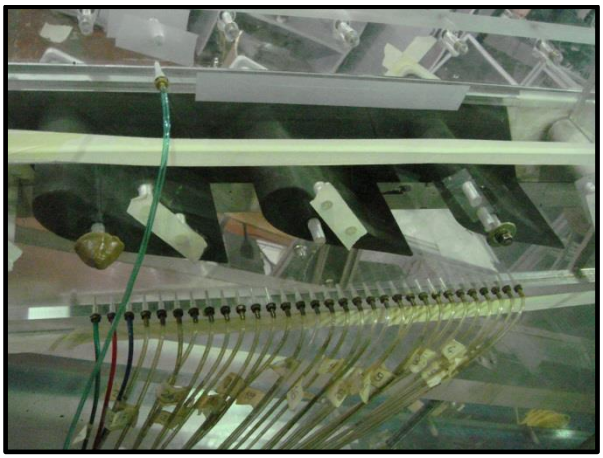

Figure 2.6 : static pressure taps downstream the cascade .

2.5 Measurement techniques for aerodynamic tests

Some tests were performed to check the flow conditions both for the cascade and the coolant injection system. In particular, cascade inlet boundary layer traverses, vane profile load distribution, and downstream pressure measurement to check the flow periodicity were performed. Cascade inlet flow condition was checked 1.6 the axial chord upstream of the vane leading edge by traversing a flattened Pitot probe to measure the inlet boundary layer profile. Moreover, a single wire DANTEC CTA hot wire anemometer was used to measure the inlet turbulence intensity level.

Vane loading was measured by means of instrumented vanes, while flow periodicity was checked using 31 pressure taps distributed along the tangential direction over about 3 vane passages, 45% of the axial chord downstream of the vane trailing edge.

A HP 3852A D.A.C.U. unit (12 bit resolution) was used to acquire all pressure (± 100 mV range) and temperature (± 0.1°C) data. The uncertainty in the *MFR* value was computed according to international standards for orifice devices (EN ISO 5167-2:2003(E)). δMFR resulted to be ± 0.04% at a value of *MFR* = 0.5% and ± 0.05% at a value of *MFR* = 2.8%.

2.5.1 LDV system

A 2D LDV system was used to study the boundary layer behavior at different locations along the vane pressure side: just downstream of both hole locations (~ 1 mm, corresponding to 3*D* downstream of the holes leading edge, where the hole coordinate system origin is located, see Table 2.4), just upstream of the cutback and close to the trailing edge (x/C_{ax} = 0.92). The light source was a 300 mW Ar+ laser. A 200 mm focal length front lens allowed to measure a volume 0.06 mm in diameter and 0.6 mm in length. Two Burst Spectrum Analyzers were used to process the signals coming from the photomultipliers. All measurements were carried out acquiring 40000 burst signals at each location in coincidence mode. Sawdust smoke was used to seed the flows, both main stream and coolant. The high number of acquired signals assured statistically accurate averages: based on a 95% confidence level, uncertainties of ±0.41% and ±0.7% for mean and RMS values, respectively, have been obtained for a turbulence intensity level of 42%. Location of boundary layer traverses is shown in Fig. 2.7. All traverses extend 2 mm perpendicularly to the vane surface and are located on the holes centerline closest to the vane mid span. Each traverse was divided into 18 measuring points whose spacing was reduced down to 0.03 mm approaching the wall. All collected data have been corrected for velocity bias and error related to velocity gradients (Karpuk and Tiedermann (1976)). A computer controlled three axis traversing system driven by stepping motors assures a probe minimum linear displacement of 10 μm. The probe can also be continuously rotated around all three axis, thus making it possible to approach the vane surface everywhere. The probe was oriented in such a way to directly measure the parallel (U) and the normal (V) velocity components, with respect to the vane surface.

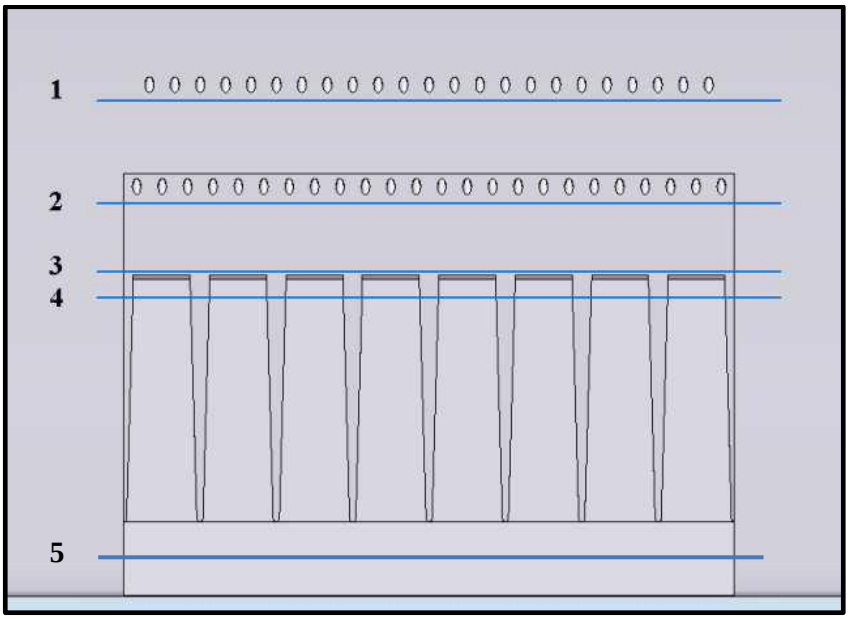

Figure 2.7: LDV measurements location .

	x/Cax
Upstream holes	0.520
Downstream holes	0.640
Cutback Upstream	0.731
Cutback downstream	0.752
Trailing Edge	0.98

Table 2.4 : LDV measurement location coordinates .

Chapter 3

Aerodynamic tests in gas turbine nozzle vane cascade

3.1 Background

In this chapter the experimental methodologies used to obtain the desired results will be described. For first the aerodynamic tests are showed, performed to study the fluid dynamic cascade behavior, and in second instance the thermal tests are exposed, used to acquire the experimental data required to calculate the convective coefficient, the reference temperature and the effectiveness. In the final part the results are discussed.

3.2 Aerodynamic measurements

In this paragraph the results of the aerodynamic measurement campaign performed to check first the general cascade operating condition and cooling system performance and then to investigate the mixing process between coolant and mainstream along the vane pressure side are presented and discussed.

3.2.1 General cascade behavior

A first set of tests was performed to characterize the wind tunnel as well as the cascade overall behavior. These tests have been all performed on the solid vane cascade with the aim of characterizing the cascade inlet flow, the flow periodicity and the blade load for variable downstream iso-entropic Mach number M_{2is}.

To characterize the cascade inlet flow field, boundary layer traverses (flattened Pitot tube) and free stream turbulence measurements (Hot Wire) were performed 1.6 C_{ax} upstream of the leading edge plane. The numerical integration of the autocorrelation function of the acquired HW signal yielded the integral length scale Λ_x. For the low Mach number operating condition, Λ_x equals 10.4 mm, while for the high Mach number case it reduces down to 6.2 mm. Fig. 3.1 and Tab. 3.1 report the boundary layer profiles and integral parameters, respectively, for variable cascade operating conditions. Even if M_{2is} significantly changes, the inlet Mach number M_1 only grows from 0.06 to 0.144. This is the reason why no significant differences were observed in the boundary layer behavior for variable cascade operating conditions, in the investigated range. This stands for all integral parameters as well as for the inlet flow turbulence intensity level, computed considering an isotropic turbulence distribution. From boundary layer profiles an inlet loss of 0.58% at M_{2is} = 0.2, that reduces down to 0.35% when M_{2is} reaches 0.6 was estimated.

Fig. 3.2 shows the downstream isentropic Mach number distributions along approximately two vane passages for variable testing conditions. These distributions were computed from inlet cascade total pressure and downstream wall tapping. Thanks to a fine tailboard adjustment, a quite good flow periodicity was obtained over the whole investigated operating conditions. In fact a quite uniform distribution can be observed at the low testing condition. Increasing the exit Mach number, a pitch wise variation can be noticed. This is due to the appearance of compressibility effects, of course more pronounced at M_{2is} = 0.6.

Finally, the measurements results of the airfoil isentropic Mach number profile at the mid span section are shown in Fig. 3.3, for variable testing conditions. The blunt leading edge is responsible for the strong acceleration up to almost $0.5c_{ax}$

along the suction side, followed by a strong diffusion up to the trailing edge. The maximum M_{is} value at $X = 0.4c_{ax}$ is about 0.9 on the suction side.

M_{2is}	M_1	δ [mm]	δ^* [mm]	H_{12}	ζ [%]	Tu_1 [%]
0.2	0.06	23.6	2.6	1.43	0.58	1.7
0.4	0.11	22.2	2.2	1.34	0.44	1.5
0.6	0.14	21.7	2.3	1.32	0.35	1.6

Tab. 3.1 : Inlet boundary layer and turbulence parameters.

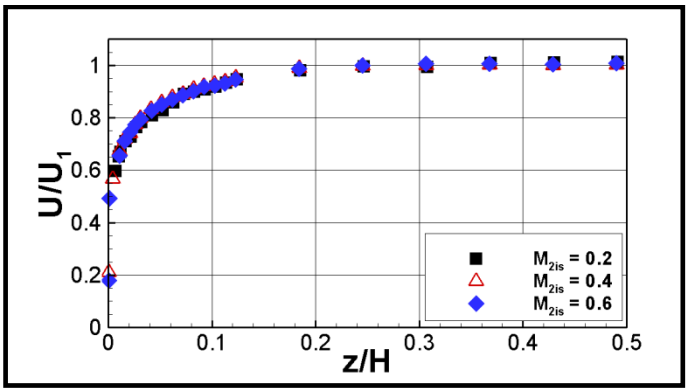

Figure 3.1 : Inlet boundary layer profile (X/c_{ax} = - 1.6).

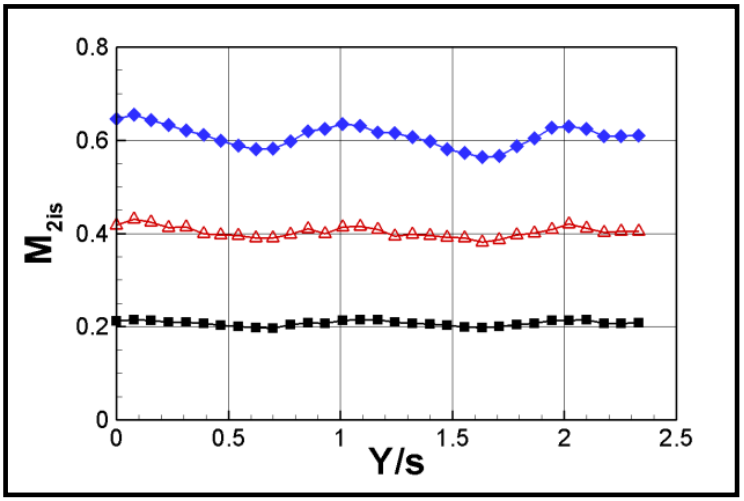

Figure 3.2 : Downstream M_{2is} distributions (X/c_{ax} = 1.45).

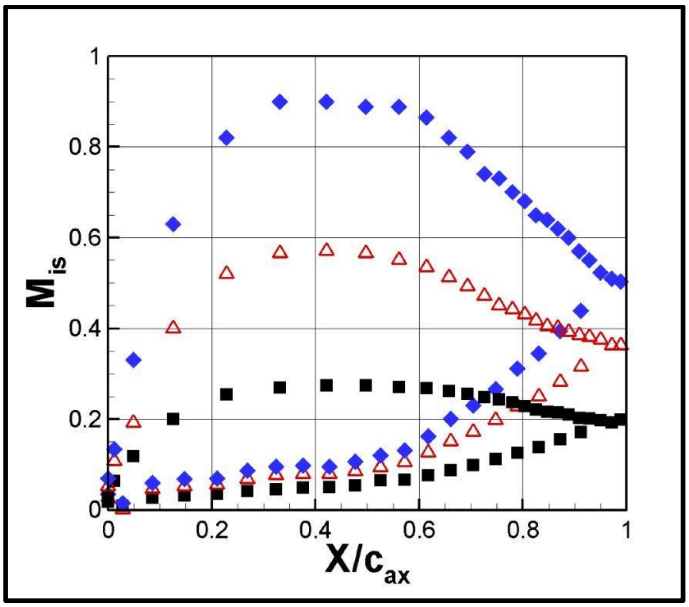

Figure 3.3 : Vane load.

No evidence of flow separation was observed, neither at the lowest tested Mach number. Along the pressure side, a moderate acceleration from the leading edge up to $0.4c_{ax}$, is followed by a much stronger acceleration up to the trailing edge. Please note that the first row is located in the region of moderate acceleration (X/c_{ax} = 0.52), while the second one (X/c_{ax} = 0.64) and the cutback (X/c_{ax} = 0.7) are located in the region of high acceleration. This, coupled with the presence of a unique plenum feeding both the cooling holes and the cutback, could negatively affect the injection condition through the first row of holes, at low injection rates. In fact, it may happen that the plenum total pressure is high enough to discharge the required amount of coolant through the cutback, but not enough to avoid main flow ingestion though the first row of holes. When this occurs, a degradation in the performance of the all cooling system is expected.

3.2.2 Cooling system characterization

Some preliminary tests were also carried out on the cooled vane cascade aiming at defining the cooling system behavior. A first set of runs were performed with only the cutback blowing by varying both the cascade operating condition (M_{2is} = 0.2 - 0.6) and the coolant to mainstream mass flow ratio *MFR*. The same tests were repeated with both holes and cutback blowing. These data were used to define the mass flow sharing among holes and cutback and the corresponding discharge coefficients. A unique mass flow as well as a unique discharge coefficient for all the

holes was computed, since it is a practical impossibility to perform tests without the cutback blowing. Figure 3.4 clearly shows that most of the coolant exits through the cutback slots. The amount of coolant discharged through the holes decreases with rising M_{2is}, at constant *MFR*, especially when compressibility effects become significant. This is consistent with the increasing pressure gradient along the rear pressure side as well as with the increasing cross flow influence, even more relevant at low pressure ratios. It should be noted that, at the largest M_{2is}, an overall *MFR* larger than 1% is required to allow holes blowing.

Based on mass flow share and measured coolant mass flow, holes and cutback coolant exit velocity were calculated and compared to the corresponding free stream velocity values. The latter were computed from the vane load distribution (Fig. 3.4), assuming that coolant injection does not significantly alter the solid vane load profile. This assumption was confirmed by Puddu et al. [3.1] who tested the same cooled vane geometry. Figure 3.5 shows the obtained velocity ratio (*VR*) values at different injection conditions, for two selected outlet Mach numbers. M_{2is} strongly influences the *VR* distributions, especially at the low *MFR*. This influence is much stronger for the two rows of holes than for the cutback. This is consistent with the much higher losses taking place inside the holes, especially at the low injection conditions. Worth to be noted is the *MFR* value for which *VR* becomes greater than unity: at the low Mach number it roughly corresponds to a *MFR* higher than 2.0 for both cutback and holes. When M_{2is} increases, the two rows of holes show increased *VR* values at low injection rates. Improved thermal performance at low injection rates are thus expected at design Mach number with respect to the low speed condition.

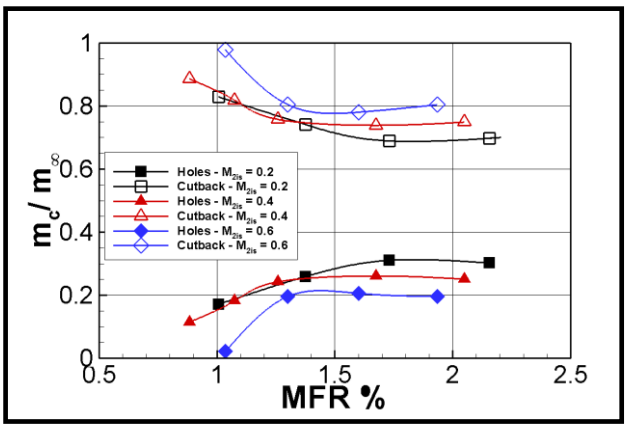

Figure 3.4. Mass flow sharing between rows and cutback.

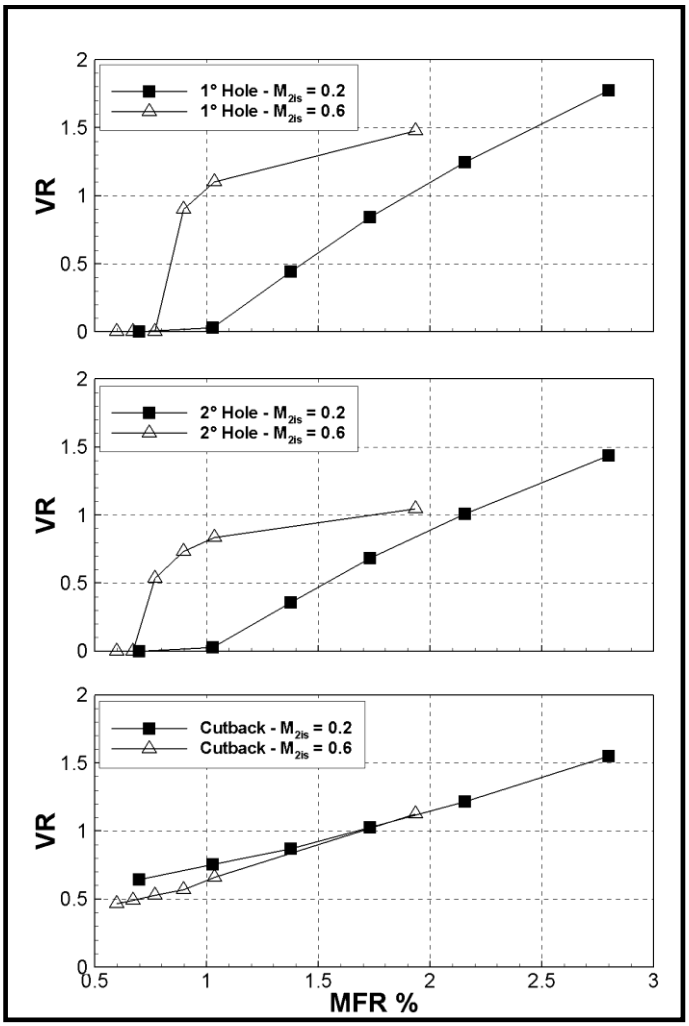

Figure 3.5 VR for holes and cutback slots.

3.2.3 Coolant to mainstream mixing process

To investigate the coolant to mainstream mixing process, boundary layer traverses were performed at four locations along the vane pressure side for a constant downstream Mach number of 0.2 and variable coolant to mainstream mass flow ratios *MFR*. The results from the LDV measurements are reported in terms of profiles of time averaged streamwise velocity component, streamwise and wall normal rms velocities and associated shear stress components. The data are normalized with respect to the local free-stream velocity (U_e).

Fig. 3.6 shows boundary layer data measured just downstream of the first row of cylindrical holes. For low blowing conditions (MFR_{hole} = 0.27%), the velocity profile in Fig. 3.6a shows that the coolant flow stays close to the vane surface with velocity values always lower than the free stream one. This evidence, associated with the absence of appreciable shear stresses and low velocity fluctuations (Figs. 3.6b-d), indicates a moderate mixing between coolant and main stream flows that, as reported in Pietrzyk et al. (1989)[3.2], is normally associated to a coolant to mainstream velocity ratio *VR* slightly lower than 1. When MFR_{hole} is increased above 0.53%, the streamwise velocity profile is characterized by a remarkable over-speed (up to $2U_e$ for the highest tested MFR_{hole} of 0.87%) whose peak is found at increasing elevations with rising injection condition. Consistently with a *VR* above one, high turbulent activity is found inside the shear layer between coolant and main stream, with velocity fluctuations as large as 40% of the free stream velocity and a certain degree of anisotropy, especially at the jet boundaries. For MFR_{hole} = 0.68% and 0.87%, slightly negative values of shear stresses are found close to the vane surface: it might indicate jet lift-off. Moreover, the high values of velocity fluctuations (see Figs. 3.6b,c) measured at increasing distances from the wall for MFR_{hole} > 0.53% are an indication of the existence of a strong mixing between coolant and main flow with consequent fast jet spread in the wall-normal direction.

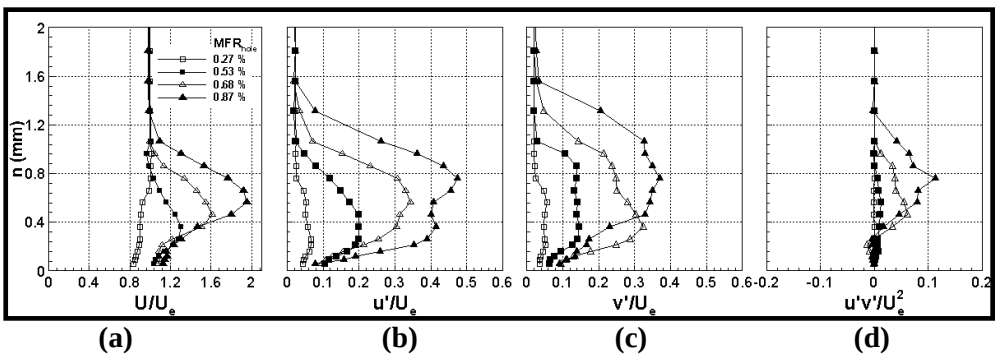

Figure 3.6 : Row #1 boundary layer profiles (s/D = 3 - hole centerline).

The LDV results for the second row of cooling holes are provided in Fig. 3.7. The streamwise velocity profiles (Fig. 3.7a) are characterized by the absence (MFR_{hole} = 0.27% and 0.53%) or the presence of a weak over-speed (MFR_{hole} = 0.68%). Only for MFR_{hole} = 0.87% a velocity peak of 1.25 U_e is reached, which is always lower than the values measured for the first row. Indeed, a similar over-speed value is obtained in the first row at MFR_{hole} = 0.53%. Therefore, it can be concluded that the *VR* for row #2 jets is always lower than the one of row #1 at

constant *MFR*. This also explains the lower turbulent activity that is measured for the downstream jets (Figs. 3.7b-d). In particular, the shear stresses are always very week and hardly detectable (Fig. 3.7d) and the streamwise (Fig. 3.7b) and wall normal (Fig. 3.7c) fluctuations have lower peak values that are localized closer to the vane surface. This is particularly evident for MFR_{hole} = 0.59% and 0.76% conditions. Moreover, it can be observed that the fluctuation values at high elevation from the wall (n > 1.2 mm) are always increasing with *MFR* and do not converge to a unique value as it occurred for row #1. This effect, which is slightly detectable also in the *U* velocity profiles, is due to the strong and rapid diffusion of the jets coming from row #1 that occurs as soon as MFR_{hole} reaches value of 0.68%.

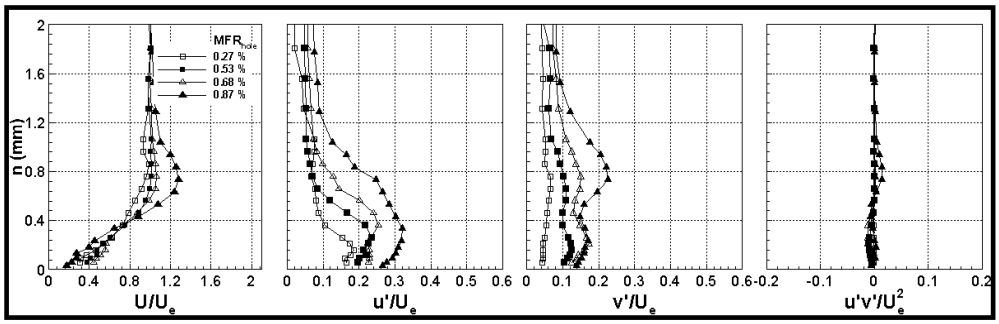

Figure 3.7: Row #2 boundary layer profiles (*s/D* = 14.5 - hole centerline).

Moving downstream, the next measuring point was located just upstream of the cutback's lip, at $0.71C_{ax}$ from the vane leading edge. To verify the degree of mixing approaching the cutback, some measurements were performed at a fixed distance from the vane surface of 1 mm, moving the measurement volume along the span. Figure 3.8 shows the streamwise and normal mean velocity components distributions for variable injection conditions. Please note that the origin of x-axis is on the mid span hole centerline. From these distribution it is clear that the mixing is not fully completed, and a certain degree of non-uniformity characterizes the flow approaching the cutback lip.

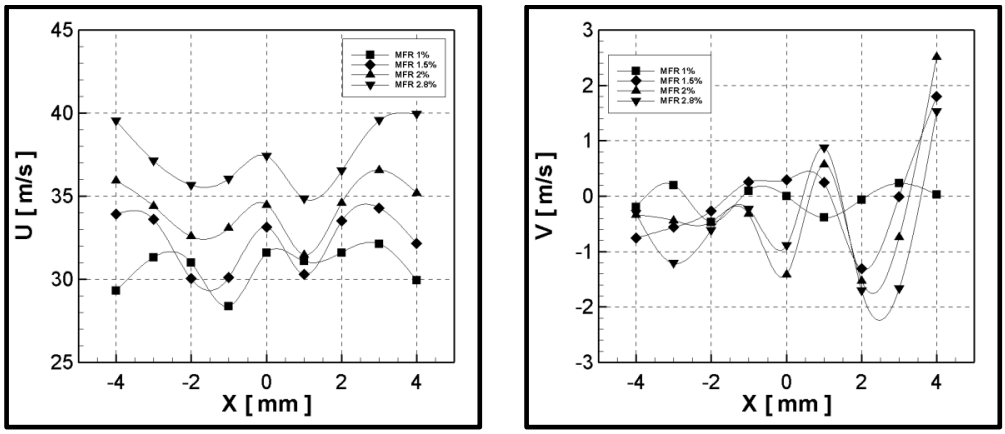

Figure 3.8 : velocity profiles upstream of the cutback lip (x/C_{ax} = 0.71).

Figure 3.9 shows the boundary layer profiles measured for the same injection conditions at x = 0 and 1 mm upstream of the cutback lip, also corresponding to the middle of the central slot. At this axial location there is mixing between the coolant flow discharged by both rows of holes. The measured boundary layer at *MFR* = 2.8% shows a reduced velocity defect, but in all cases the boundary layer profiles always show a turbulent behavior.

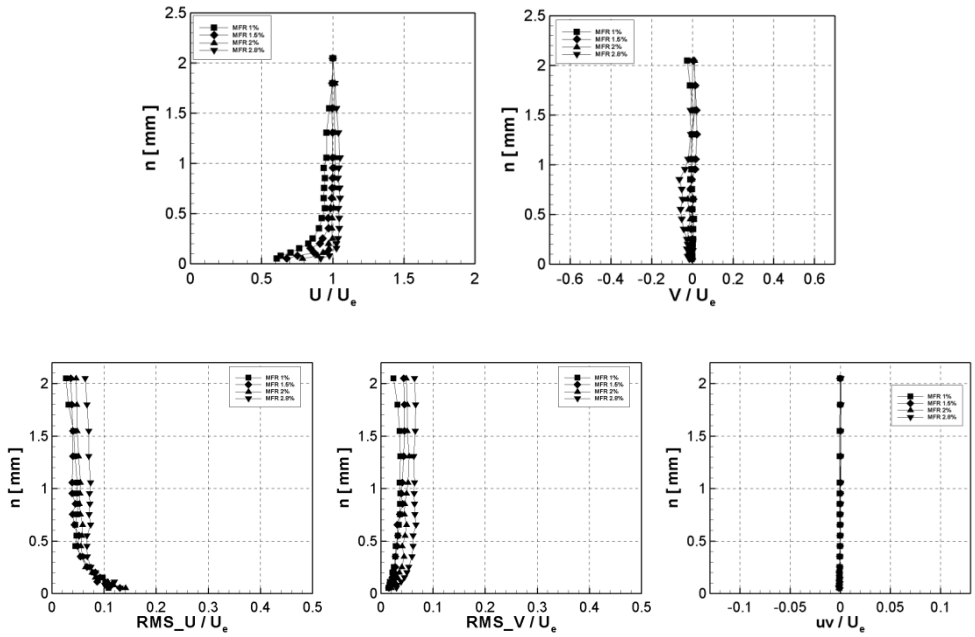

Figure 3.9: boundary layer profiles upstream of the cutback lip (x/C_{ax} = 0.71).

The PS boundary layer approaching the TE was also investigated for variable injection conditions at constant M_{2is} = 0.2 (Fig. 3.10). The reported mean velocity and streamwise velocity fluctuation component distributions show that the cutback geometry is responsible for a relevant boundary layer modification approaching the TE. The boundary layer appears to be turbulent for all the tested *MFR* values, including the no blowing condition. The gradual increase in *MFR* from 1.0% to 2.8% was found to be responsible for a progressive re-energization of the boundary layer: in particular, for the highest *MFR*, the U/U_e ratio indicates an over speed at a distance from the wall between 0.5 and 1.5 mm. As far as the streamwise turbulence is concerned, the cutback is confirmed to deeply affect the boundary layer profile. The behavior of u'/U_e by varying the *MFR* can be explained through the mixing process between the coolant and the main stream flow. Considering the case at *MFR* = 0.0% as a reference, the injection of a small amount of coolant (*MFR* = 1.0%) does not significantly alter the turbulence level close to the wall (n < 1 mm). With a further increase in *MFR* up to 2.0% the streamwise turbulence is reduced: the coolant is injected into the mainstream with a velocity close to the mainstream one. This condition assures the best interaction of mainstream and coolant flow. With a further increase in *MFR* up to 2.8%, the coolant velocity is higher than the stream wise one: the mixing process is inevitably associated with an increase in turbulence level.

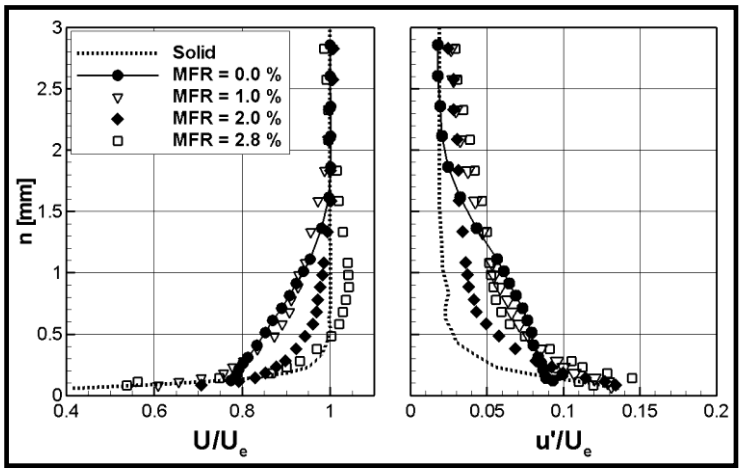

Figure 3.10. PS boundary layer traverses (X/c_{ax} = 0.92) for variable *MFR* at M_{2is} = 0.2.

Chapter 4

Heat transfer coefficient and effectiveness

4.1 Introduction

In the literature various methods are available to characterize the convective heat exchange performance. Especially for problems where the temperature differences are quite small (enough to consider the fluid's thermo-fluid dynamic parameters to be constant) and in those cases where there is no phase transition, it is possible to define an appropriate convective heat transfer coefficient *h*, that is a function of fluid flow field. In the present chapter some of those techniques are presented that allows to find the *convective heat transfer coefficient* and the *cooling effectiveness*. In particular, a steady technique is first presented, followed by the unsteady techniques. The last one of who, has been used in the present thesis to evaluate h and η.

4.2 Two and three temperature problems [2.1]

The simplest problem that is possible to find talking about external forced convective heat transfer is the *two temperature problem*. Where there is a surface which is cooled (or heated) by a fluid stream that flows over it. In that case the main parameters that govern the phenomenon are the fluid's and the surface's temperatures (*two temperature*) and the heat transfer coefficient *h*. So the local heat flux is conventionally expressed as:

$$q = h_R(T_w - T_\infty) \tag{4.1}$$

where T_∞ is the mainstream temperature, that renders h_R independent of the temperatures. Such choice of that temperature reduces the convection coefficient h_R to a function of aerodynamic character of the flow field alone, and allows local surface convection behavior to be condensed into that constant of proportionality for a given flow field. In the following discussion, linear convection behavior is assumed, with the temperature differences sufficiently small to allow fluid properties to be represented by values independent of the temperature. In two temperature problems, the *reference temperature* is simply the fluid temperature T_∞, and convection experimentation consists of measuring q together with T_w and T_∞ and from them determining h_R .

Three temperature convection arises naturally in many situations where a material surface's temperature and heat flux are influenced by adjacent mixing of two fluid streams. Such situations occur frequently in modern systems and devices such film cooling or heating, where a secondary fluid is injected trough a surface to displace and mix with the primary stream flowing over it. Indeed in many devices, especially those operating at high temperature, an accurate knowledge of the boundary condition on the flow bounding walls is vital to successful and durable design.

In these kind of problems, the reference temperature is at some generally unknown level, that depends on the supply temperature of the two interacting streams, and the degree of mixing that has occurred between them, before they are adjacent to the various locations of the surface; both h_R and T_{ref} must be considered unknowns. But please note that the reference temperature must be equal to the wall temperature when the heat exchanged is zero, i.e. in adiabatic wall condition. This means that the reference temperature in a three temperature problem is the so called adiabatic wall temperature.

Another possibility is to express the heat transfer coefficient by using :

$$q = h_3\left(T_{film} - T_w\right) \tag{4.2}$$

where the convection coefficient is based on the average temperature of both fluid streams (*film temperature,* T_{film}) and it is no longer a function of the aerodynamic flow field alone.
Coupling the two heat flux expressions, it is possible to introduce two non-dimensional ratios:

$$\frac{h_3}{h_{ni}} \qquad and \qquad \Theta = \frac{T_{film} - T_\infty}{T_w - T_\infty} \tag{4.3}$$

where T_{film} ,in this study assumed equal to T_c , which is the coolant temperature. The relationship between these two parameters was translated in a graphical representation by Metzger and Mitchell in 1966 (Fig. 4.1).

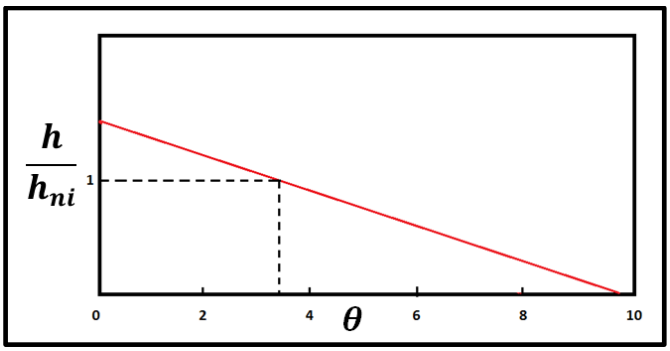

Fig. 4.1 : Film cooling performance representation .

It is important to observe that the intersection of the line on the ordinate is the convection coefficient h_{ni} in the situation where the secondary fluid temperature is identical to the mainstream temperature, but both fluids are present. This situation is different from the case where only the mainstream is present, and thus, this point represents a different situation from the two temperature problem . The intersection point on the abscissa is the reciprocal of the temperature difference ratio, usually called *film cooling effectiveness η (4.4)* :

$$\eta = \frac{T_{Ad,w} - T_\infty}{T_c - T_\infty} \tag{4.4}$$

Indeed, this point represents the situation with *q=0,* or better: the case of Adiabatic wall ($T_{Ad,w}=T_w$).

It has to be recognized that fig. 4.1 represents a three temperature performance at a single location on the surface, so in general, *Adiabatic Wall Temperature* and *convection coefficient* vary on the surface, yielding a family of lines like this, with both intercepts varying with location.
In either instance, three temperature convection performance, including heat and adiabatic aspects, can be established by any two points on the line (Metzger, et al, 1968) , determined by measurement of local surface-averaged quantities.

4.3 Steady method

If the surface heat flux is known (q), it is possible to made a steady analysis of the convective heat transfer coefficient. Indeed, once that the system has reached steady conditions, it will be sufficient to acquire the wall temperature, and the fluid driving temperature to directly obtain h.

$$h = \frac{q}{(T_{ref} - T_w)} \tag{4.5}$$

The main difficulty of steady methods is to generate a known heat flux, i.e. a heat flux as uniform as possible over the whole surface of interest. This is a major concern when working with complex geometries. Another concern is the evaluation of heat losses. Trying to overcome these problems, transient techniques have been proposed.

4.4 Transient technique

4.4.1 Problem formalization

In their paper, Vedula and Metzger determine two points of the figure 4.1 curve performing transient tests, where test surface, initially at a uniform temperature at all depths, is suddenly exposed to steady mainstream and secondary flows and the transient response is indicated by the color display of a thin coating of liquid crystals. In a two temperature problem, the surface's response is governed by a semi-infinite formulation of the transient heat conduction equation with the following boundary and initial conditions:

$$\begin{cases} \dfrac{\partial T}{\partial t} - \alpha \dfrac{\partial^2 T}{\partial^2 z} = 0 \\ -k \left[\dfrac{\partial T}{\partial z}\right]_{z=0} = h_R\left(T_w - T_{ref}\right) \\ [T]_{z=0} = T_i \\ [T]_{t=0} = T_i \end{cases} \tag{4.5}$$

Where α is the *thermal diffusivity* :

$$\alpha = \frac{k}{\rho C_p} \tag{4.6}$$

This semi-infinite description is appropriate as long as the transient temperature does not exceed the thickness of the wall material being used.
As told before, in this study both the convective coefficient and the reference temperature (the adiabatic wall temperature) are unknown, so this is a reverse problem, because the temperature time distribution is known by the experimental tests, while the research goals are the boundary conditions.
However, the convection coefficient is constant with time and, for the situations where T_{ref} is known, the solution (Carslaw and Jaeger, 1959) is given by :

$$\frac{T_w - T_i}{T_{aw} - T_i} = 1 - exp[h^2 \xi(t)] erfc\left[h\sqrt{\xi(t)}\right] \tag{4.7}$$

Where the time depending function $\xi(t)$ that has been introduced for convenience of writing :

$$\xi(t) = \frac{\alpha \cdot t}{k^2} \tag{4.8}$$

By measuring the time *t* required for the surface temperature to reach a prescribed value displayed by an indicating coating, *h* can be determined directly from equation (4.7), as demonstrated by Clifford, et al (1983), Ireland and Jones (1986), Metzger and Larson (1986), and Saabas, et al (1987).

This solution can be extended to a three temperature problem, where the reference temperature T_{ref} is unknown. In the next sections how to obtain a simultaneous solution for both the unknown parameters is described.

4.4.2 Single transient test

The idea is to perform one experimental test, and to extract from this the surface temperature history during an appropriate time interval. Therefore chosen two temperature levels, for example T_{green} and T_{blue} (where green and blue are the corresponding Thermochromatic Liquid Crystal color), and the corresponding times to achieve these temperature levels (t_{green} and t_{blue} respectively) it is possible to proceed with the solution of the system (4.9) :

$$\begin{cases} \dfrac{T_{w,green}-T_i}{T_{aw}-T_i} = 1 - exp\left[h^2\xi\left(t_{green}\right)\right] erfc\left[h\sqrt{\xi\left(t_{green}\right)}\right] \\ \dfrac{T_{w,blue}-T_i}{T_{aw}-T_i} = 1 - exp\left[h^2\xi\left(t_{blue}\right)\right] erfc\left[h\sqrt{\xi\left(t_{blue}\right)}\right] \end{cases} \tag{4.9}$$

Since the experimental data should satisfy the numerical solution (4.7), it follows that two points taken over the same curve, must have the same parameters h and T_{aw}.

4.4.3 Two separate transient test

An alternative is represented by the following method, where two different tests are performed, using two different flow temperatures, and maintaining constant all the other parameters (like the injection conditions). Hence, chosen one temperature level for both tests (as example T_{green}) the two different achievement time (t_1 and t_2) are acquired. It has to be noted that, with respect to the (4.9) solution, in this case the unknown parameters are three: h , T_{aw_1} and T_{aw_2} , due to the different flow temperature bringing different reference temperatures; in order to proceed with the solution it is necessary to find a third equation.
Considering the two non-dimensional ratios (4.3), it follows that both cases must have the same intercept value with the abscissa, so :

$$\frac{T_{c\_1}-T_{\infty,1}}{T_{aw,1}-T_{\infty,1}} = \frac{T_{c\_2}-T_{\infty,2}}{T_{aw,2}-T_{\infty,2}} \tag{4.10}$$

As a consequence (4.10) will be the third equation in system (4.11):

$$\begin{cases} \frac{T_{w,green}-T_i}{T_{aw,1}-T_i} = 1 - exp\left[h^2\xi\left(t_{green,1}\right)\right]erfc\left[h\sqrt{\xi\left(t_{green,1}\right)}\right] \\ \\ \frac{T_{w,green}-T_i}{T_{aw,2}-T_i} = 1 - exp\left[h^2\xi\left(t_{green,2}\right)\right]erfc\left[h\sqrt{\xi\left(t_{green,2}\right)}\right] \\ \\ \frac{T_{c\_1}-T_{\infty,1}}{T_{aw,1}-T_{\infty,1}} = \frac{T_{c\_2}-T_{\infty,2}}{T_{aw,2}-T_{\infty,2}} \end{cases} \quad (4.11)$$

4.4.4 Duhamel's superposition theorem

The two methods just described, are valid only for test surfaces, initially at a uniform temperature, and *instantaneously* exposed to a hot fluid flow, in order to have a true step change. Unluckily this "true step" is impossible to obtain in an experimental test, and for this reason the solution (4.7) used in both the systems (4.9) and (4.11) is replaced through the use of the *Duhamel's superposition theorem*. Forward the actual gradual change is obtained by using a series of steps. Defined a time interval τ_i , it is possible to write a time-dependent function $U(t-\tau_i)$:

$$\boldsymbol{U(t-\tau_i) = 1 - exp[h^2\xi(t-\tau_i)]erfc\left[h\sqrt{\xi(t-\tau_i)}\right]} \quad (4.12)$$

Then is necessary to define another time-dependent function which relates the time variation in T_∞ , T_c and the value of η in each time step τ_i :

$$\Delta T_{aw} = (1-\eta)\Delta T_\infty + \eta \Delta T_c \quad (4.13)$$

At this point equation (4.7) can be written in discrete terms:

$$T_w - T_i = \sum_{i=1}^{N} U(t-\tau_i)\cdot \Delta T_{aw} \quad (4.14)$$

Form equation (4.14) it is possible to note that (4.13) corresponds to the first term in the denominator in (4.7). Now the two equations system can be solved iteratively for the two unknowns.

4.5 Selected approach

In the present work an alternative way to calculate the convective coefficient and the reference temperature has been selected. This method force the numerical solution (4.7) to return that h and T_{aw} values which minimize the square error against the experimental data. In this way a single test is required, but the whole time history of the wall surface is used, and not only two instants, improving the measurement accuracy. To do this a post processing procedure was developed in order to transform the discrete data set in a continuous low, allowing the use of a numerical method to achieve the solution in reasonable time. To test the code, developed in MATLAB, a preliminary theoretical investigation was carried out.

4.5.1 Preliminary study

In this section a theoretical study is described, where experimental data are simulated using an exact solution, calculated from equation (4.7); subsequently some random noise has been added. In table 4.1 the input data are summarized:

Convective Coefficient	87	W/m^2*K
Initial Temperature	25.5	°C
Reference Temperature	47	°C
Noise spread	±0.1	°C
Test Time	300	s

Table 4.1 : Input data for the theoretical study .

Two representative curves are shown in figure 4.2: the exact solution and the simulated experimental data, i.e. the exact solution with noise superimposed.

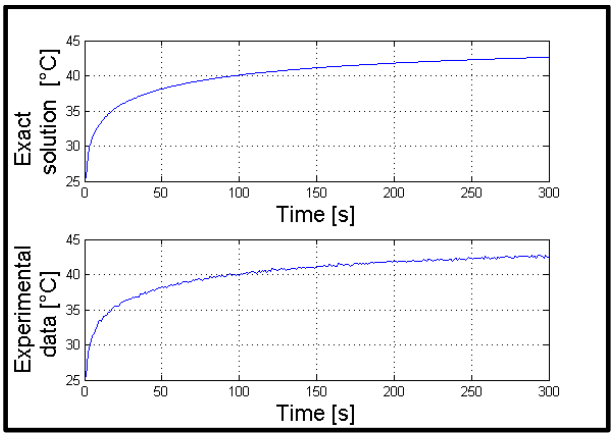

Figure 4.2 : Exact solution (up) and Temperature with 0.1 noise added (down).

4.5.2 Data Filtering and Fitting

Accepting figure 4.2 data as experimental, an *Adaptive Wiener filter* [2.2] has been applied. This function consists in an adaptive filtering procedure based on statistics estimated from the neighborhood of each data value. By defining the local mean and variance around each discrete temperature data using the following equation:

$$\bar{T} = \frac{1}{N \cdot M} \sum_{i \in \pi} T(X_i, Y_i) \tag{4.15}$$

$$\sigma^2 = \frac{1}{N \cdot M} \sum_{i \in \pi} T^2(X_i, Y_i) - \bar{T}^2 \tag{4.16}$$

$$var = \sqrt{\frac{\sum_{i \in \pi} [T(X_i, Y_i) - \bar{T}]^2}{N \cdot M}} \tag{4.17}$$

Where π is the NxM local neighborhood of each discrete temperature data value, *var* is the *noise variance*; so the restored two dimensional signal estimated by the Wiener filter will be:

$$T_{Filtered}(X_i, Y_i) = \bar{T} + \frac{\sigma^2 - var^2}{\sigma^2} \cdot [T(X_i, Y_i) - \bar{T}] \tag{4.18}$$

The adjective *"Adaptive"* means that the π-domain reduces its dimensions close to the matrix boundaries; this allows to include the border values too, avoiding the

bother to reduce the data size; the price to pay back is an inferior accuracy in that areas due to the reduction of the local π-domain.
Since in the present work a local thermal history is studied, hence a linear vector, the filtering domain π is reduced to a single line (1,M) where compute the statistical values.
The next step is represented by finding the best fit curve with the filtered data. This step has been performed using *"curve fitting"* toolbox from MATLAB®, where the most similar power low is selected as type of fit (4.19).

$$T(t) = a \cdot t^b + c \tag{4.19}$$

That toolbox returns as output the coefficient values *a*, *b*, *c* .

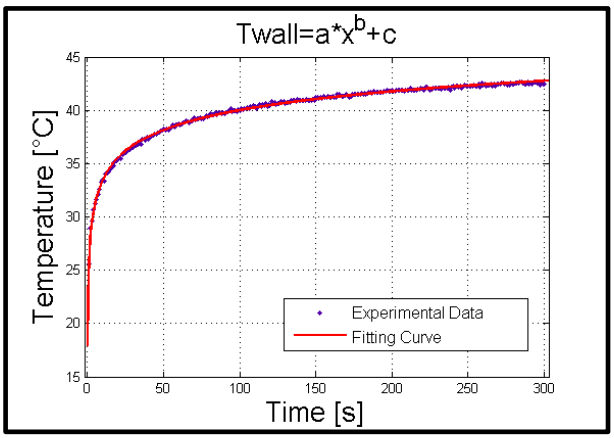

Figure 4.3 : Experimental filtered data (blue dots) and fitting curve (red line) .

Note that the fitted curve is very close to the data set, and can be used in the next step as input data. The convenience of MATLAB® toolboxes is the possibility to generate an m-file from the user interface, to be reused in MATLAB® functions or macros.

4.5.3 Error Analysis

From equation (4.7) it is possible to obtain a more suitable form of the solution for this study (4.20) :

$$T_w(t) = T_i + (T_{aw} - T_i) * \left(1 - exp[h^2 \xi(t)] erfc\left[h\sqrt{\xi(t)}\right]\right) \tag{4.20}$$

Indeed now it is possible to couple that equation with equation (4.19), in order to obtain a single equation in two variables, assuming:

$$T_{Fitting}(t) = T_w(t) \tag{4.21}$$

From this point the fitting errors will influence the solution too. It is important, hence, to choose the right sampling time to acquire data, in order to minimize this contribution. It would be appropriate at this point to introduce the *"Error"* definitions:

1. ***Mean Error:*** $\overline{Error} = \frac{T_{Fit}(t) - T_w(t)}{Time}$ (4.22)

2. ***Mean Square error:*** $SqrEr = \frac{[T_{Fit}(t) - T_w(t)]^2}{Time}$ (4.23)

These errors are calculated over a predefined range of h and T_{aw} obtaining the respective error surfaces showed in figures 4.4-5 :

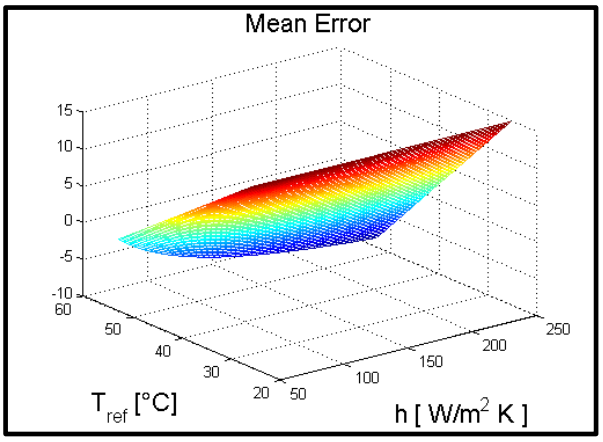

Figure 4.4 : Mean error surface .

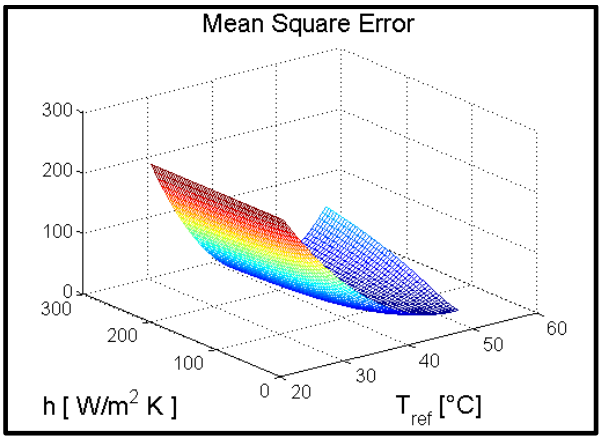

Figure 4.5 : Mean Square Error .

Changing the point of view it is possible to clarify the ideas about these two surfaces.

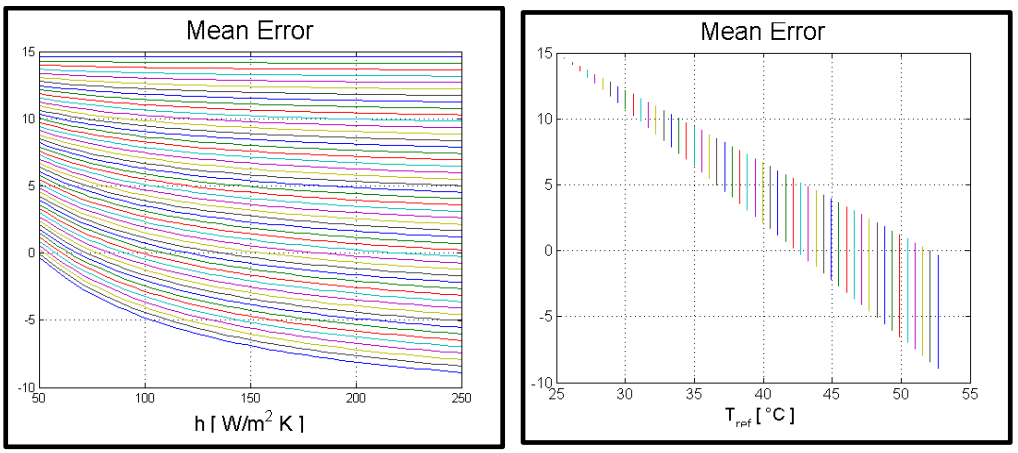

Figure 4.6 : Mean Error surface from side plans .

Observing figure 4.6 it is clear that the *Mean Error* doesn't present any minimum point, but it is a surface that passes through the *Mean Error=0* plane. This means that it could be possible to obtain T_{aw} by a bisection method, knowing *a priori* the convective heat transfer coefficient. This is also confirmed from the linear dependence of T_w with respect to T_{aw} in equation (4.20). Unfortunately it is most common that h is unknown.

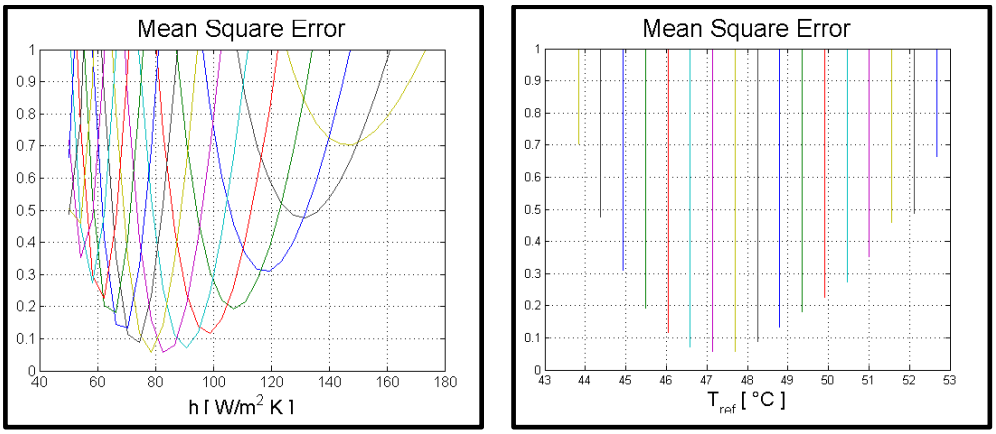

Figure 4.7 : Square Error surface from side plans.

As a second instance, observing the *Square Error* surface from the side planes it is clear that a minimum exists, in particular this point has coordinates close to *h* and T_{aw} true values, goals of the method.

As for the curve fitting, to find the minimum point of the square error surface, a MATLAB® toolbox has been used. In particular the *Optimization toolbox* with a constrained nonlinear algorithm has been chosen, and the only constrain selected is to find the local minimum point in a user defined range for *h* and T_{aw} values (*"Interior point"*).

The application of the optimization algorithm returns the researched coefficients affected by a small error :

h	81.9116	W/m^2*K
T_{ref}	47.32	°C

Table 4.2 : Heat Transfer governing parameter calculated using the least squares method for the proposed case .

Superposing the Temperature-Fitted curve, with the one obtained using the results it is easy to see that the two lines are very close one to the other (fig. 4.8) while the error introduced by the fitting with respect to the raw data, and the error introduced by that method with respect to the fitted data are extremely low as shown in figure 4.9 . That means that in this case the method is efficient.

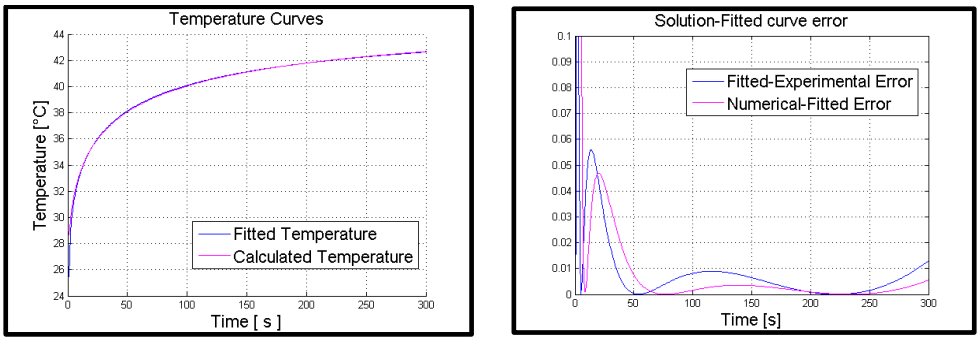

Figure 4.8 : on the left side the superposition of the fitted and calculated curve, on the right side the confront between the error introduced by fitting and by the numerical method.

4.5.4 Method Accuracy

As shown in the precedent section, for this problem the solution is acceptable, but will it be for other values of *h* and T_{aw} too? To answer this question, a new calculation has been performed to check the sensitivity to each parameter, with respect to the variation of the other. In particular, fixed one value for *h*, T_{aw} has been changed in an appropriate range, and *vice versa*. In figure 4.9-10 the relative errors over *h* are shown, defined as:

$$\%\ \boldsymbol{Error\_h} = \frac{\boldsymbol{h}_{\boldsymbol{Exact}} - \boldsymbol{h}_{\boldsymbol{Calculated}}}{\boldsymbol{h}_{\boldsymbol{Exact}}} \tag{2.24}$$

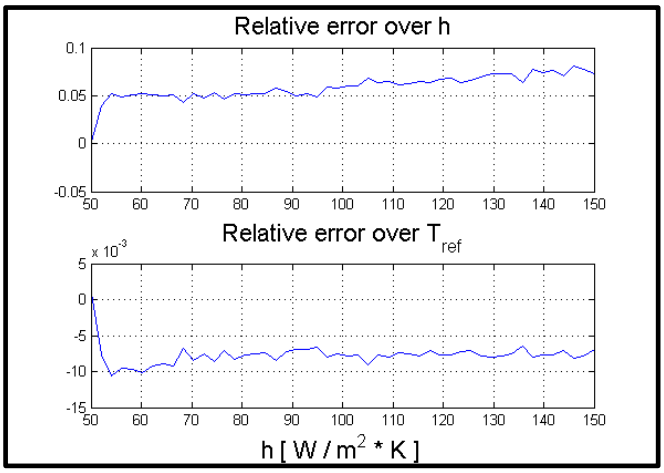

Figure 2.9 : Relative error of *h* and $T_{ref} = T_{aw}$ over the convective coefficient variation .

And the relative error calculated over the T_{aw} variation :

$$\%\ \boldsymbol{Error\_T_{ref}} = \frac{\boldsymbol{T}_{\boldsymbol{Exact}} - \boldsymbol{T}_{\boldsymbol{Calculated}}}{\boldsymbol{T}_{\boldsymbol{Exact}}} \tag{2.25}$$

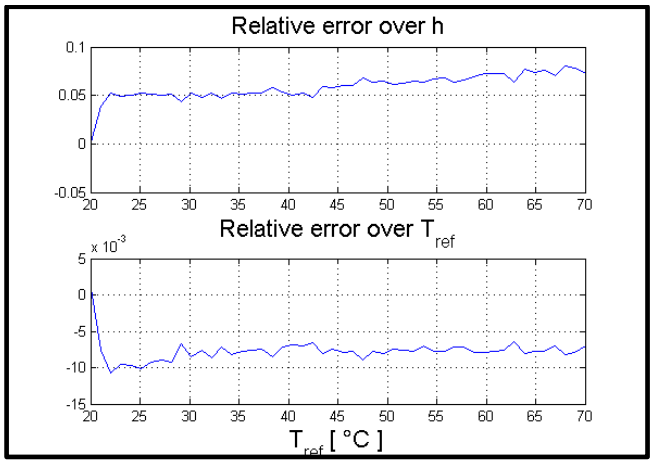

Figure 4.10 : Relative error of $T_{ref} = T_{aw}$ and h over the reference temperature variation

.

From this short analysis, it is possible to say that an error of about 5% for h and one lower than 0.01% on T_{aw} could be considered acceptable, so that the exposed method is not only precise, but robust too.

Chapter 5

Thermal measurement on the cutback trailing edge cascade

5.1 Introduction

In this section the experimental methodology to find the *convective heat transfer coefficient* and the *Effectiveness* in a first stage stator linear cascade is described. It must be considered that in this situation, the blade thickness is very small, hence it is important to know not only the pressure side temperature distribution (the directly cooled surface), but the suction side temperature too. Indeed, as exposed in chapter 4, those methods are valid if the heat flux doesn't exceed the material thickness. By removing the inlet filter, it is possible to use TLC to detect the cutback temperature distribution using a CCV camera situated on top (fig. 5.1). The suction side temperature has been detected using the IR camera.

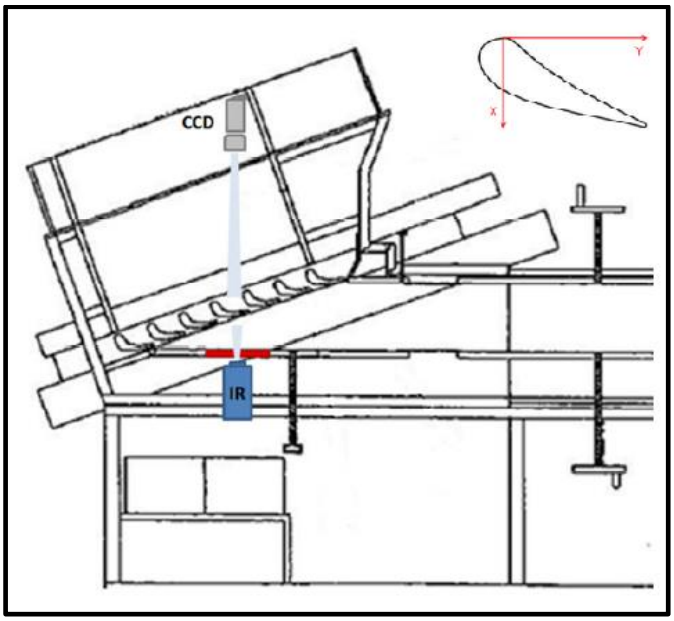

Figure 5.1 : Wind Tunnel experimental set-up .

5.2 Color theory

In this chapter the optical techniques adopted to measure the surface temperature and the adiabatic effectiveness will be presented, so it is convenient to spend some time to introduce the reader to digital image encoding. The most common and used is the RGB system. It is based on a tridimensional space, where the three independent coordinates are the *Red*, *Green* and *Blue* quantities, variables from 0 to 1. In other words, the pixel color is a function of these three quantities and colors can be represented on a cubic space (fig. 5.2).

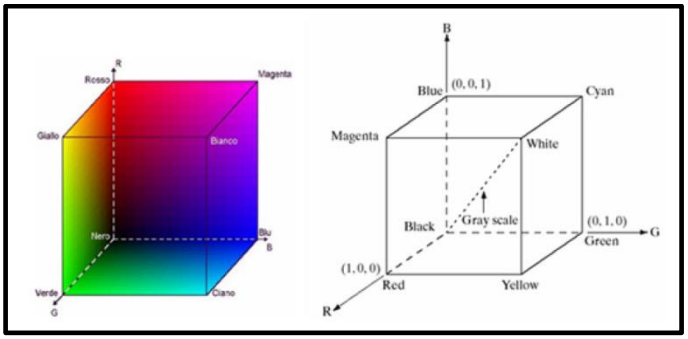

Figure 5.2 : RGB model color space .

It is worth to note that the principal diagonal represents the gray scale, where white is (0,0,0) and black is (1,1,1). This model reproduces as close as possible the human way to see, indeed in our eyes there are two types of light receptors: the first (*rods*) is responsible of the intensity only in condition of low light; while there are three type of *cones* that works in high illumination situations, which are responsible of the color perception, in particular *red*, *green* and *blue* respectively. The problem of this color model is related to the high number of information it gives, that strongly depend on the light intensity. As consequence of that, by using RGB color model, could result that the same body has two different color, cause it depends from the lighting conditions. It is, hence, necessary to find another way to codify images, a way that is able to separate the different contribution of light and color. To do this the HSI color model is conventionally used, that involves three different parameters: *Hue*, *Saturation* and *Intensity*, that are defined as:

- **Hue :** it depends from the dominant wavelength and indicates the color, as a gray scale which values go from 0 to 255;
- **Saturation :** it indicates the quantity of white radiation with respect to the color's one; a low saturation means that in the whole amount of the detected light there is a low quantity of color radiation;
- **Intensity :** it says the total radiation's magnitude

HSI is a tridimensional space too, but its shape is composed by two cones with the common basis (fig. 5.3):

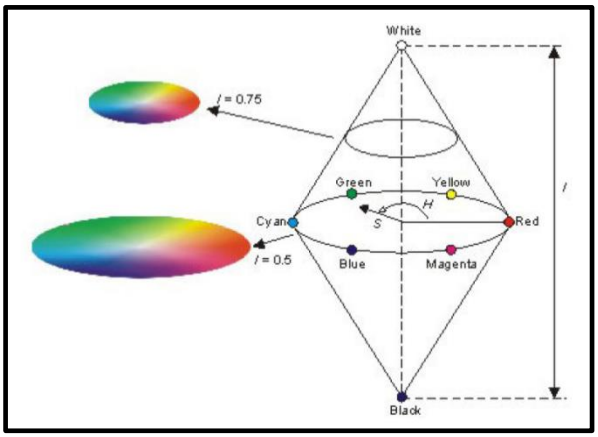

Figure 5.3 : HSI model color space .

In this space *Hue* is the angular coordinate and describes uniquely the color, from values that goes from 0 to 255; *Intensity* is the vertical axis, and defines the gray scale, indeed white in this system has coordinates equal to (0,0,255) while black

(0,0,0); at least there is the *Saturation*, which is represented as the radius magnitude and has values that goes from 0 to 1 as the Intensity.

5.3 Thermochromatic Liquid Crystal

5.3.1 Introduction to TLC

Thermochromatic liquid crystals are organic substances (chiral nematic) able to selectively reflect the light, depending on their temperature, if properly illuminated. To perform thermal tests, two types of *Thermochromatic Liquid Crystals (TLC)* have been used: *wide band TLC* which are able to detect a large temperature range (about 10 °C) which are used pure, with the aim to obtain temperature maps on the whole test surface; and *narrow band TLC*, characterized by a reduced operative range (about 1°C). This kind of TLC are usually mixed with other having different temperature range, in order to obtain a thermal sensible paint with the ability to show the isothermal lines on the surface.

5.3.2 Wide band calibration

A TLC Calibration, possibly performed in-situ, is always necessary, to define the relationship between temperature and color (HUE). To do this, a rectangular calibration plate (Aluminum made) has been used, coated with a black paint as base, and subsequently sprayed with TLCs A temperature gradient along the calibration plate was then generated by placing an electrical resistance on one side and a water cooled channel on the opposite side of the calibration device (fig 5.4). This temperature gradient was captured by means of 10 T-type thermocouples installed just underneath the model surface. The whole calibration device was in turn previously calibrated using boiling water and melting ice. TLC images were acquired by using both a CCD camera, with a 767x573 pixels resolution, respectively. The primary lighting system consists of two 150 W white light sources, each one connected to two optical fibers.

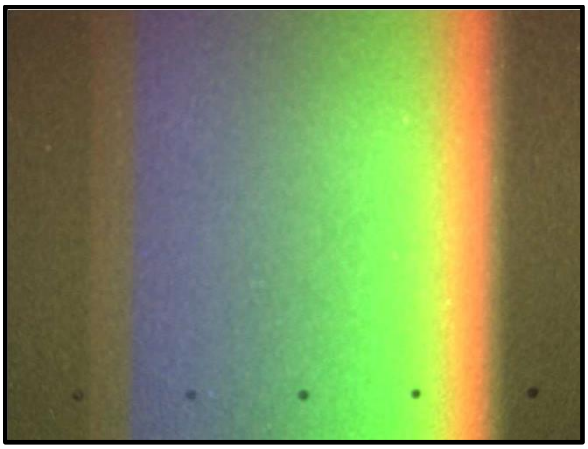

Figure 5.4 : Calibration board thermal map, note the thermo couple positions, showed by the black points .

The acquired image have to be converted, as first, from RGB to HSI codification, from which only the *Hue* component will be extracted. This because it is necessary to correlate each single color to one temperature value in order to obtain a suitable calibration curve (fig. 5.5) .

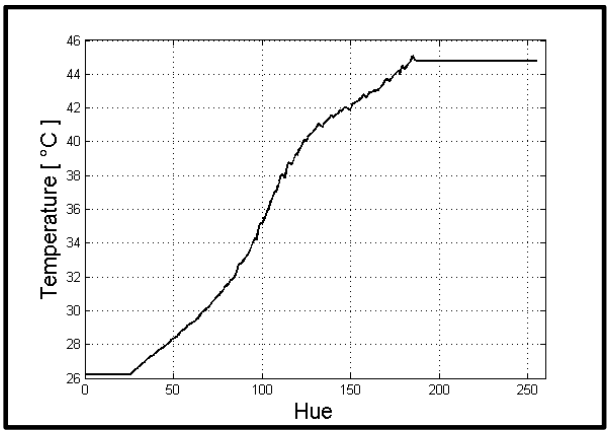

Figure 5.5 : wide band TLC calibration curve.

Is easy to note that the hue range is not complete, but the useful bandwidth only covers HUE values as large as 120-150.
All calibrations were performed in the dark, in order to eliminate any influence of background illumination. Moreover, an illumination intensity as uniform as possible was provided to the model surface by properly orienting the optical fibers, in the meanwhile avoiding any light reflection onto the camera.

5.3.3 IR camera

IR camera is a new way to detect superficial temperatures, in a non-intrusive way, indeed it doesn't require application of any type of coating or superficial treatment. It is obviously preferable if the surface is black coated, in order to avoid unwished reflections, but it is not strictly necessary. The University's camera is a *ThermoVision® A40 M* produced by *FLIR System®*. It uses a FPA (*Focal Plane Array*) sensor, with an uncooled micro bolometer having a 320 x 240 pixel resolution. Internal temperature is continuously monitored to avoid thermal distortions due to the uncooled sensor, and each time that ambient temperature changes of about 1°C, an auto calibration device makes an automatic compensation. Its maximal acquiring frequency is 25 Hz, while the spectral sensible range goes from 7.5 to 13 μm. Thermal accuracy is about ±2°C, if ambient temperature is between 5°C and 45°C. IR camera thermal sensitivity is 80 mK at an ambient temperature of 25 °C. *ThermaCAM Researcher Professional®* is the software that the camera uses as user interface.

5.3.4 IR Camera calibration

This device needs to be calibrated each time that a test begins, and it is extremely important that an *in-situ* calibration is performed. Indeed, as will be described in this section, the signal acquired not only depends on the body's surface temperature, but also on a series of parameters:

1. Ambient temperature : it is necessary to evaluate the minimum detectable temperature from the camera;

2. Transmittance coefficient : sometimes, it is necessary to interpose a glass or a lens between the investigated surface and the camera to insulate the test section. Hence, it is important to know how this external component influences the measurements: the optic's transmittance coefficient and its temperature are the parameters that are needed. The first one is required to know the entity of the radiation reduction, while the second is required to subtract from the input radiation the portion due to the optic's temperature.

3. Reflected temperature : this parameter considers the radiation portion due to the reflected radiation from the tested surface, that comes from the surrounding surfaces. Indeed, the radiation detected from the camera is the sum of the emitted and the reflected one. To subtract this contribution, it is sufficient to crumple and uncrumple an aluminum sheet, put it over the test area. That kind of surface has extremely low emissivity, and very high reflectivity, and hasn't a unique reflection plane; hence what the IR camera will acquire is only the reflected temperature.

4. Emissivity : to evaluate this parameter, two thermocouples are attached to the studied surface, hence ε is manually corrected till the IR camera and the thermocouples detect the same temperature (figure 5.6).

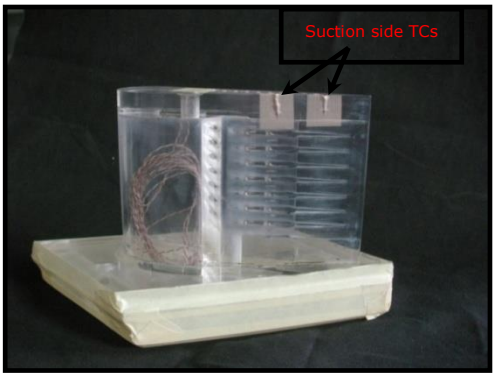

Figure 5.6: Plexiglas® airfoil and thermocouples applied on its suction side .

Unfortunately, the Plexiglas® who's composed the tunnel is opaque to the infrared wavelength, hence an optical window has been installed just facing the central vane suction side. This special IR transparent glass is made in Zinc-Selenium (fig. 5.7-8) with a transmittance of about 0.99 at ambient conditions. moreover it has an anti-reflections coating, to avoid an additional contribution to the acquired image.

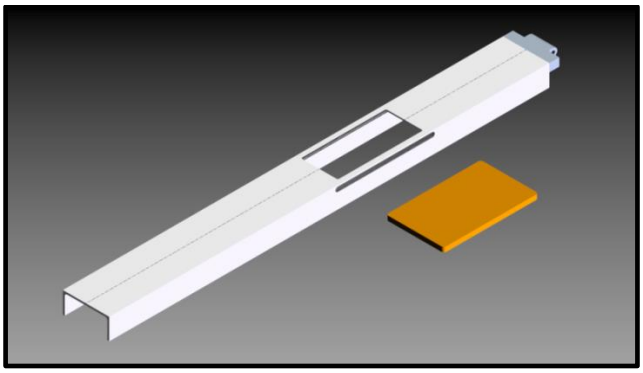

Figure 5.7: steel tailboard, optical window (orange) and its housing .

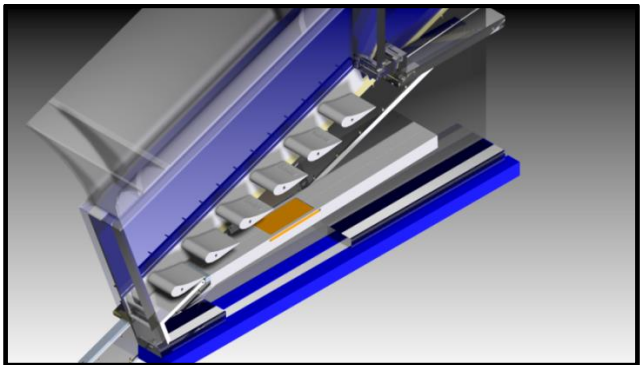

Figure 5.8 : A wind tunnel with new tailboard section .

5.3.5 Thermal Data Post-processing

Once that data has been acquired, it is necessary to choose the right portion of the airfoil, where the convective coefficient and the reference temperature (fig. 5.9) have to be calculated.

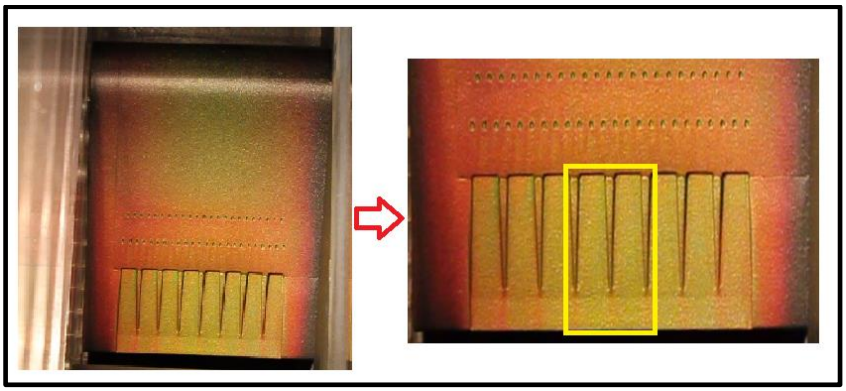

Figure 5.9 : Cutback region of interest .

Indeed, to evaluate the desired parameters using the exposed techniques, only the cutback area has been selected. Moreover it is important to choose a portion of the airfoil as far as possible from the endwalls, in order to avoid the boundary effect due to the thermal conduction.

5.3.6 Suction Side Data analysis

Once the experimental data collected, each acquired time series has been checked to control the correctness of the procedure. To do this, six points on the cutback surface has been chosen as well as their counterparts on the suction side as showed in figure 5.10.

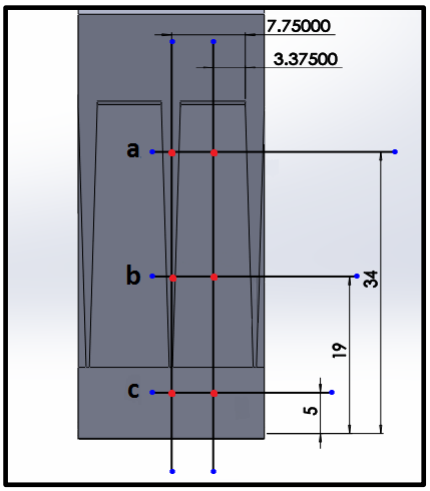

Figure 5.10 : Sample points on the cutback surface .

In figure 5.11 – 5.15 it is possible to observe the different behavior of pressure and suction side for each *MFR* tested. The red line represents the central slot's line, while the blue one is the fin point thermal evolution.

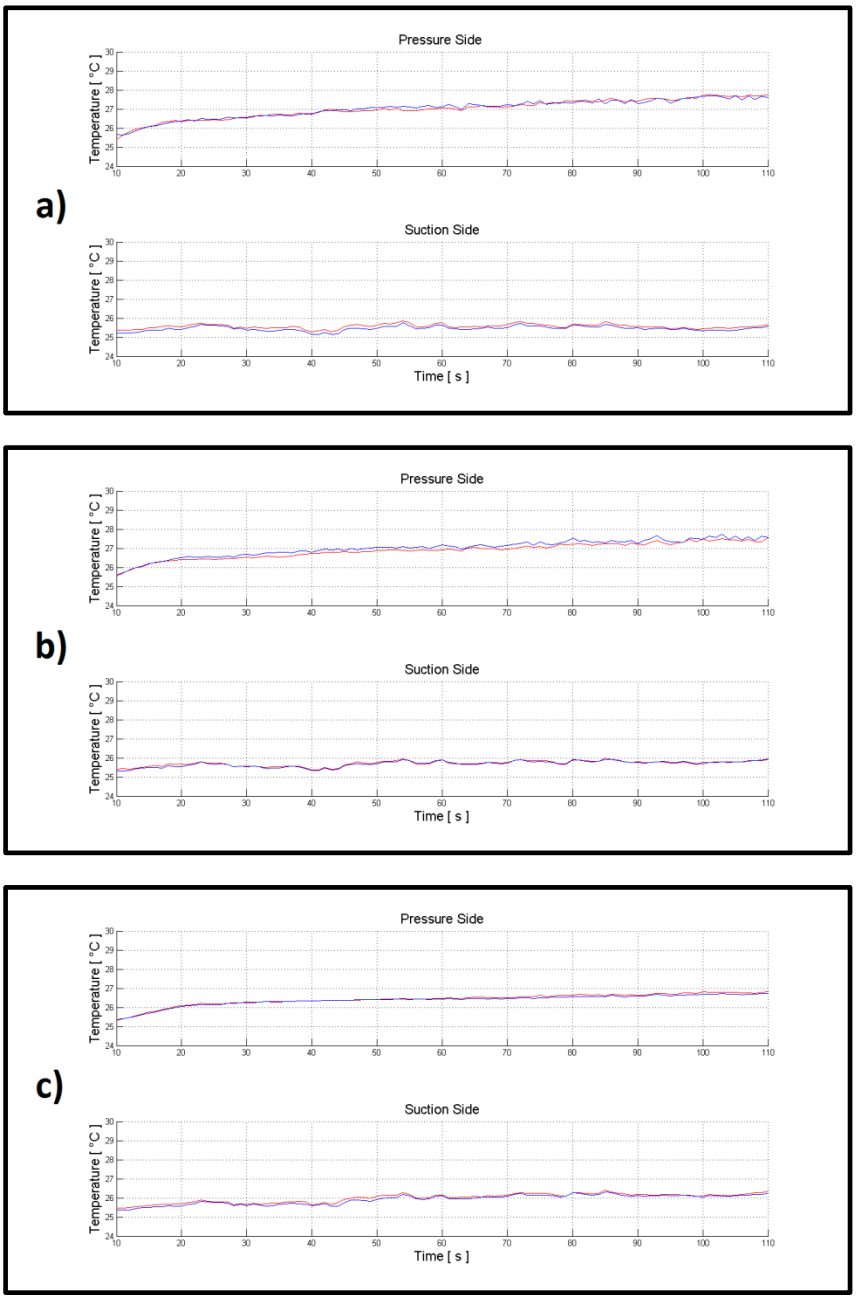

Figure 5.11 : Thermal evolution for MFR 1 .

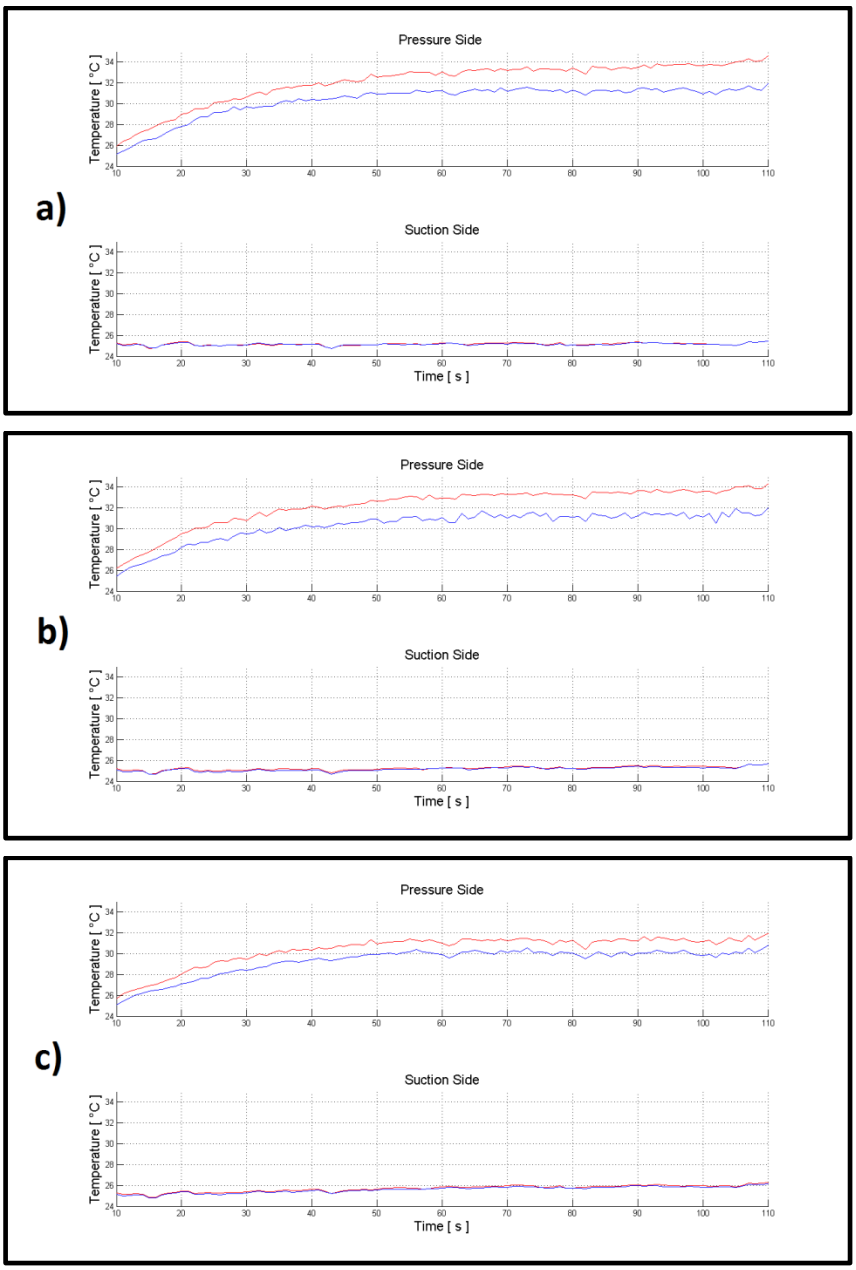

Figure 5.12 : Thermal evolution for MFR 1,5 .

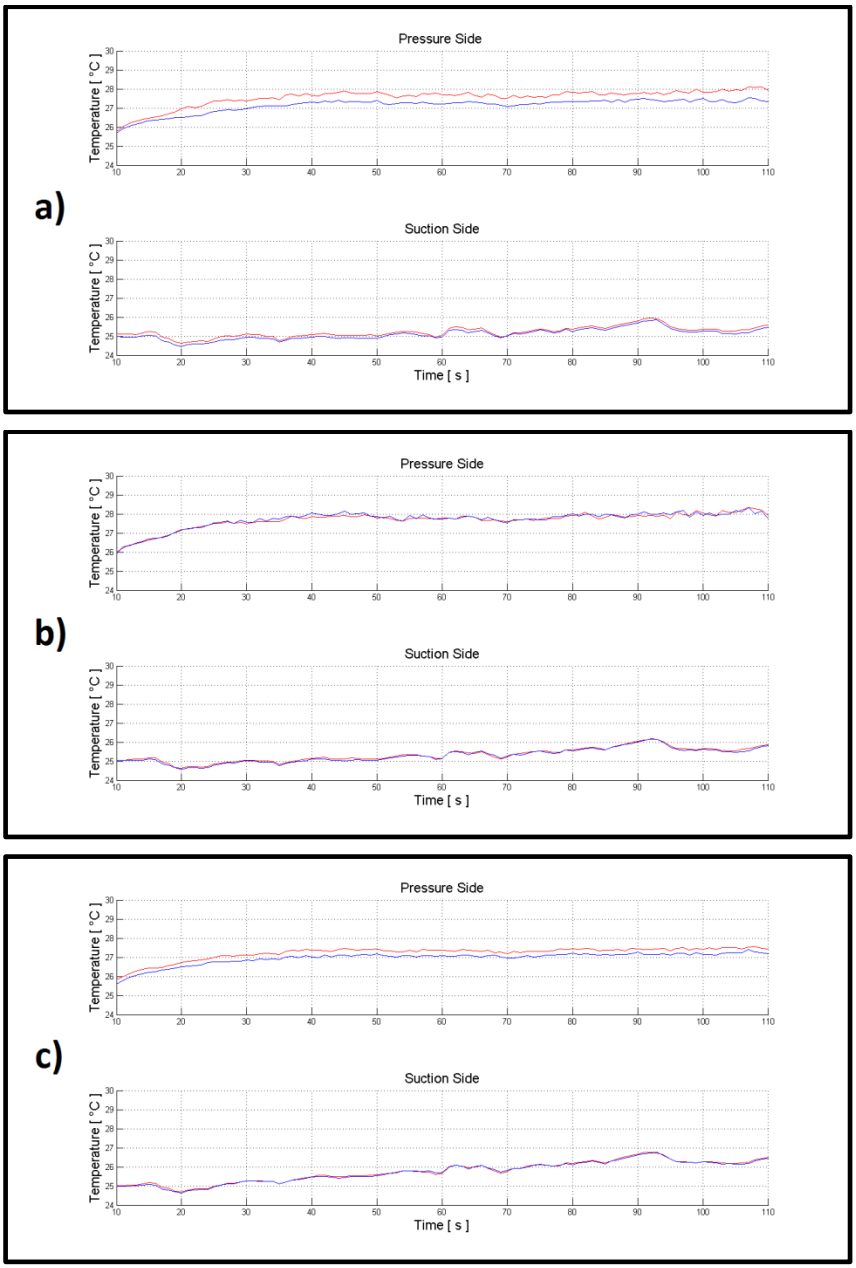

Figure 5.13 : Thermal evolution for MFR 2 .

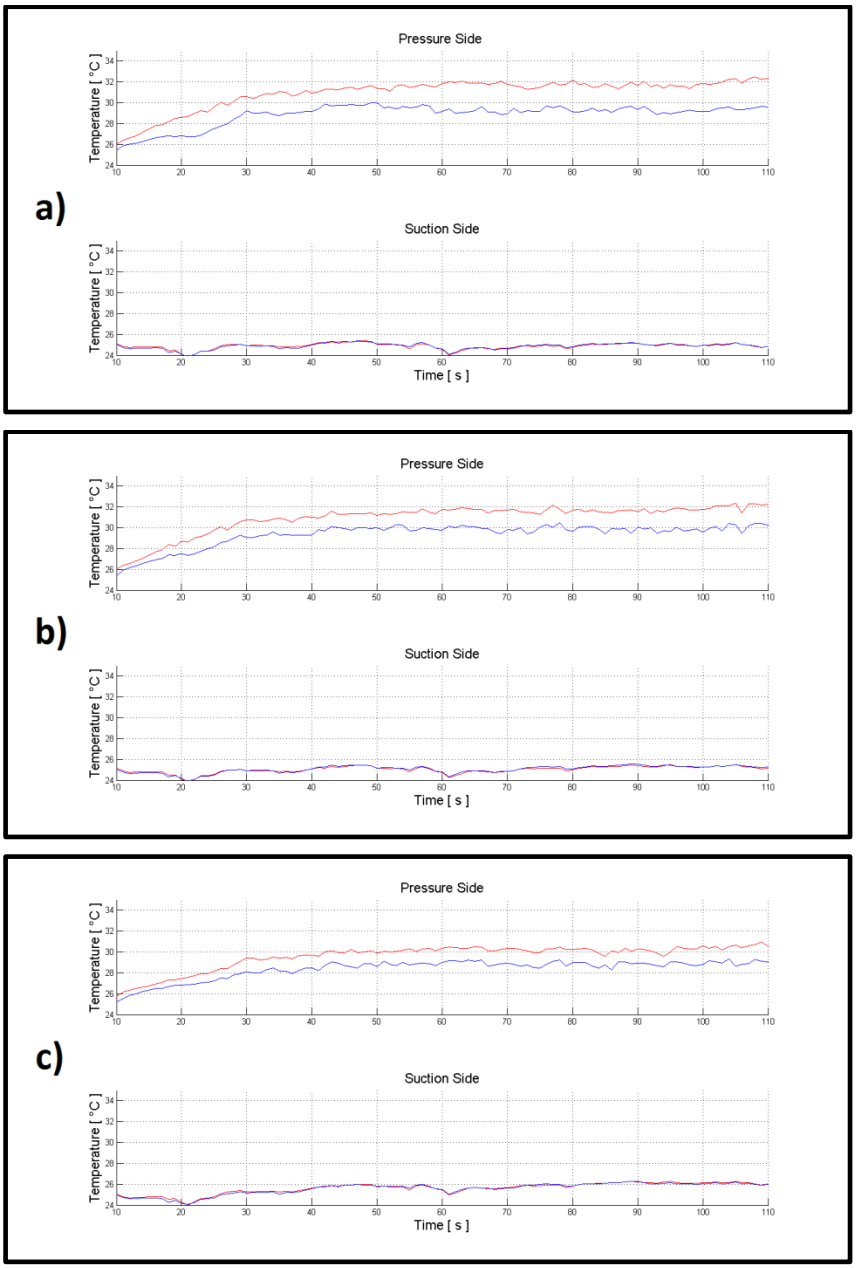

Figure 5.14 : Thermal evolution for MFR 2,7 .

Temperature time variation has been plotted starting from the 10th second from the test beginning, till the 60th. This because in the first seconds before the injection, TLC gives some spurious data, while 50 seconds are enough to perform the

calculation in reasonable time. Moreover, graphics show that for each injection condition, for pressure side's temperature variations of about 5 °C, correspond suction side's variations of less than one degree. For this reason, it has been chosen to apply the least square method used for the flat plate, to the linear cascade too.

5.4 Results

5.4.1 Convective coefficient

In this section the results coming from the application of the least square method to a linear cascade, at different injection conditions, are showed. *Convective Coefficient Maps* (fig. 5.15 - 16) are first shown:

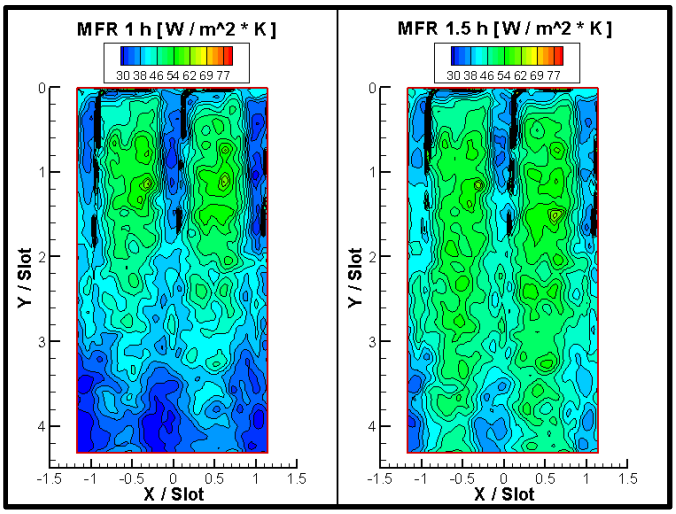

Figure 5.15 : convective coefficient maps for MFR 1 and 1,5 .

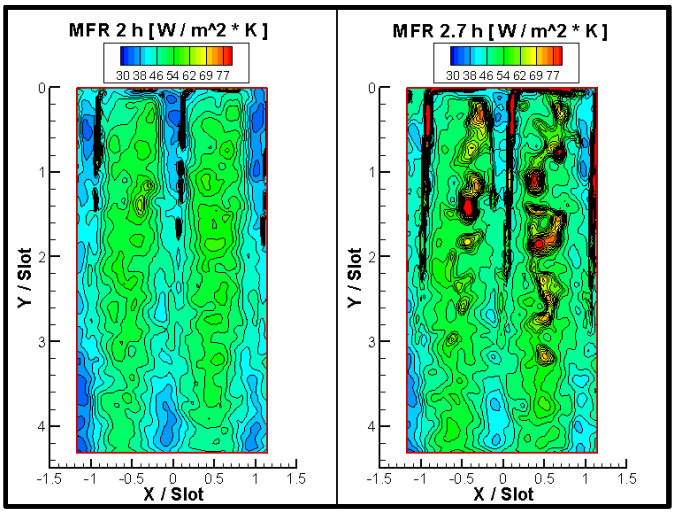

Figure 5.16 : convective coefficient maps for MFR 2 and 2,7 .

In second instance, as second least square method result, the *Adiabatic wall Temperature Maps* are obtained (fig. 5.17 - 18):

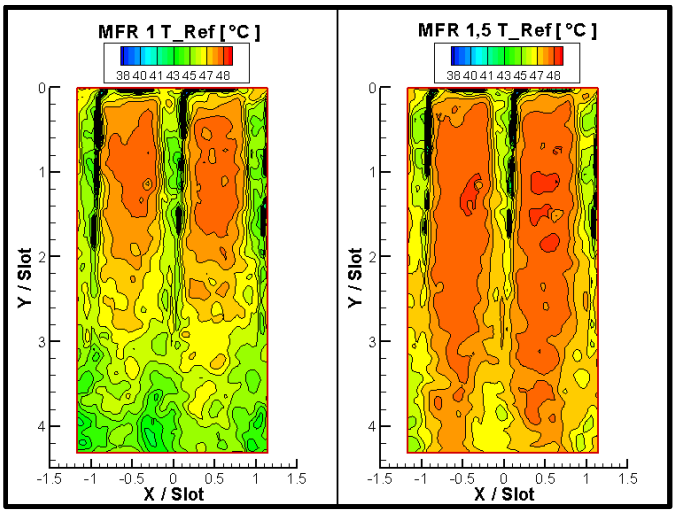

Figure 5.17 : Reference temperature maps for MFR 1 and 1,5 .

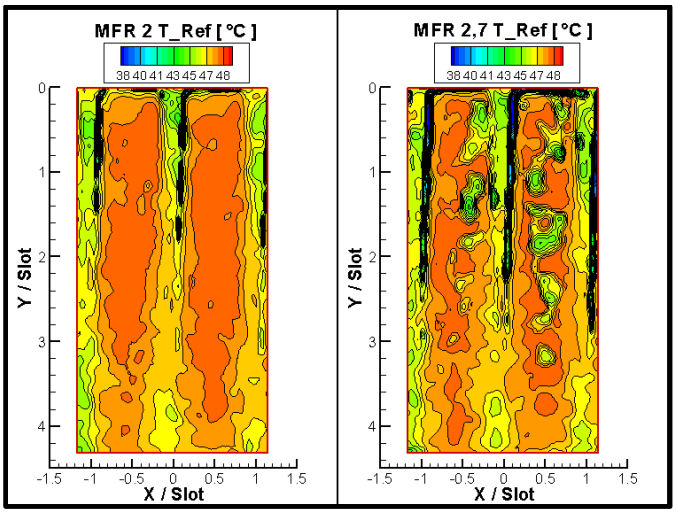

Figure 5.18 : Reference temperature maps for MFR 2 and 2,7 .

5.4.2 Film Cooling effectiveness

Film cooling effectiveness presented in this section has been calculated by using the next formula:

$$\eta = \frac{T_{aw} - T_{\infty}}{T_C - T_{\infty}} \tag{5.1}$$

where T_{∞} is the ambient temperature, equal to 25 °C, and T_C is equal to 50 °C. In figure 5.19 - 20 the effectiveness maps are presented for each mass flow rate.

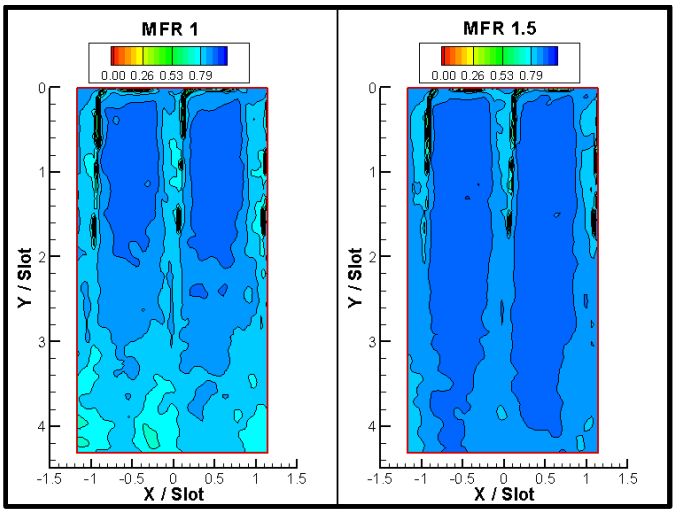

Figure 5.19 : Cooling effectiveness for MFR 1 and 1,5 .

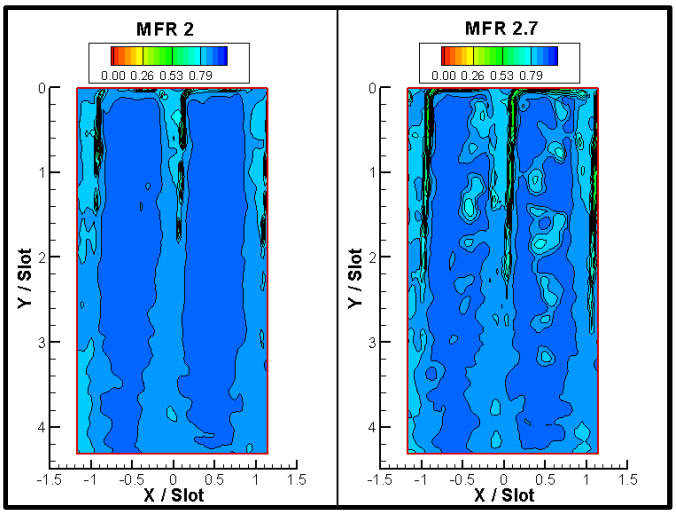

Figure 5.20 : Cooling effectiveness for MFR 2 and 2,7 .

5.5 Error Analysis

In order to measure the least square method consistency, it is important to compare the experimental wall temperature, against the numerical wall temperature obtained using the calculated *convective coefficient* and the *Reference Temperature*. In figures 5.21 - 24 the thermal histories of the cutback's points showed in figure 5.10 are shown. The experimental data are represented in blue, while in red are the numerical results.

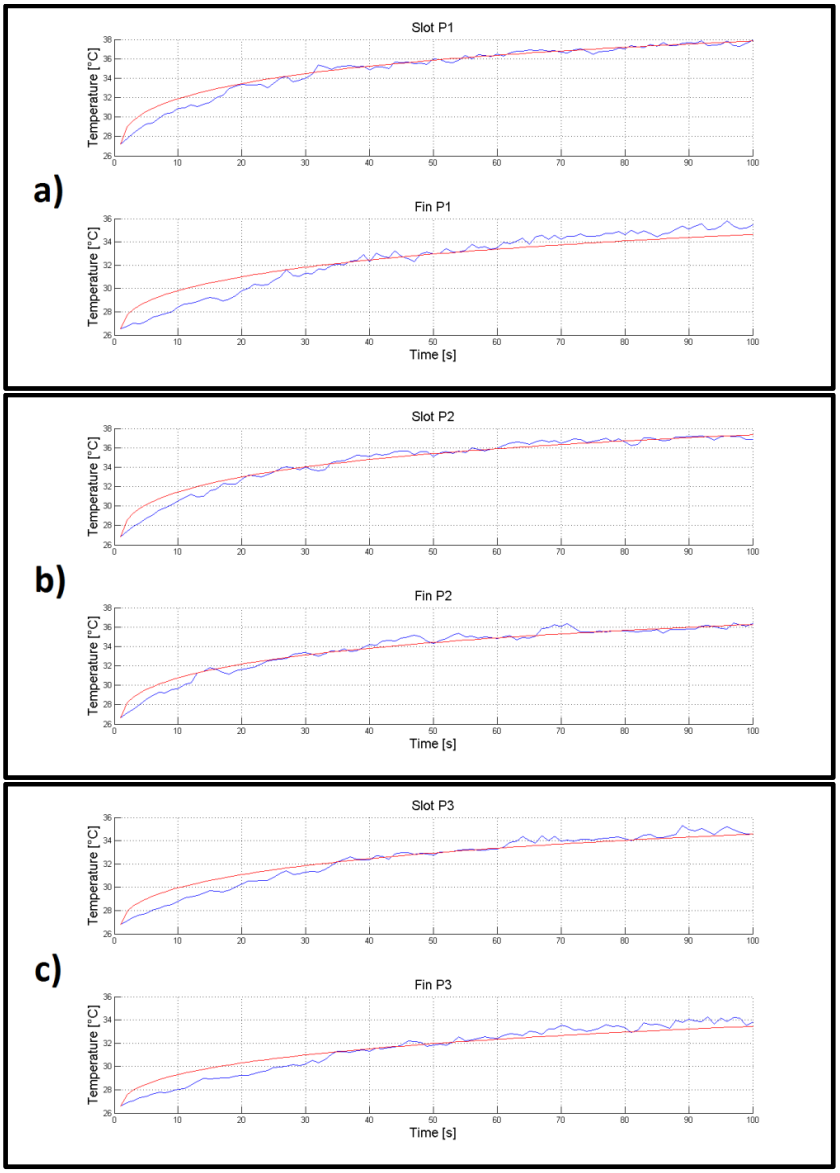

Figure 5.21 : Comparison between the experimental data and numerical for MFR 1 .

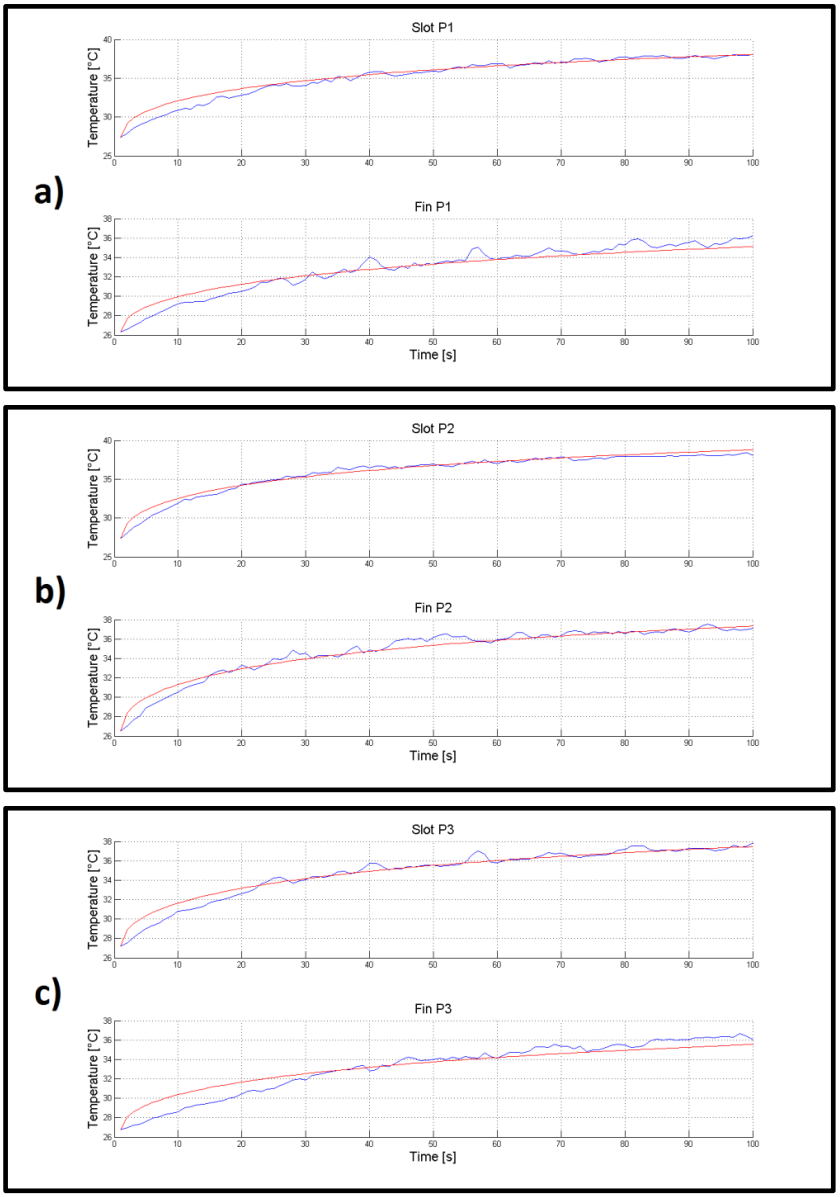

Figure 5.22 : Comparison between the experimental data and numerical for MFR 1,5 .

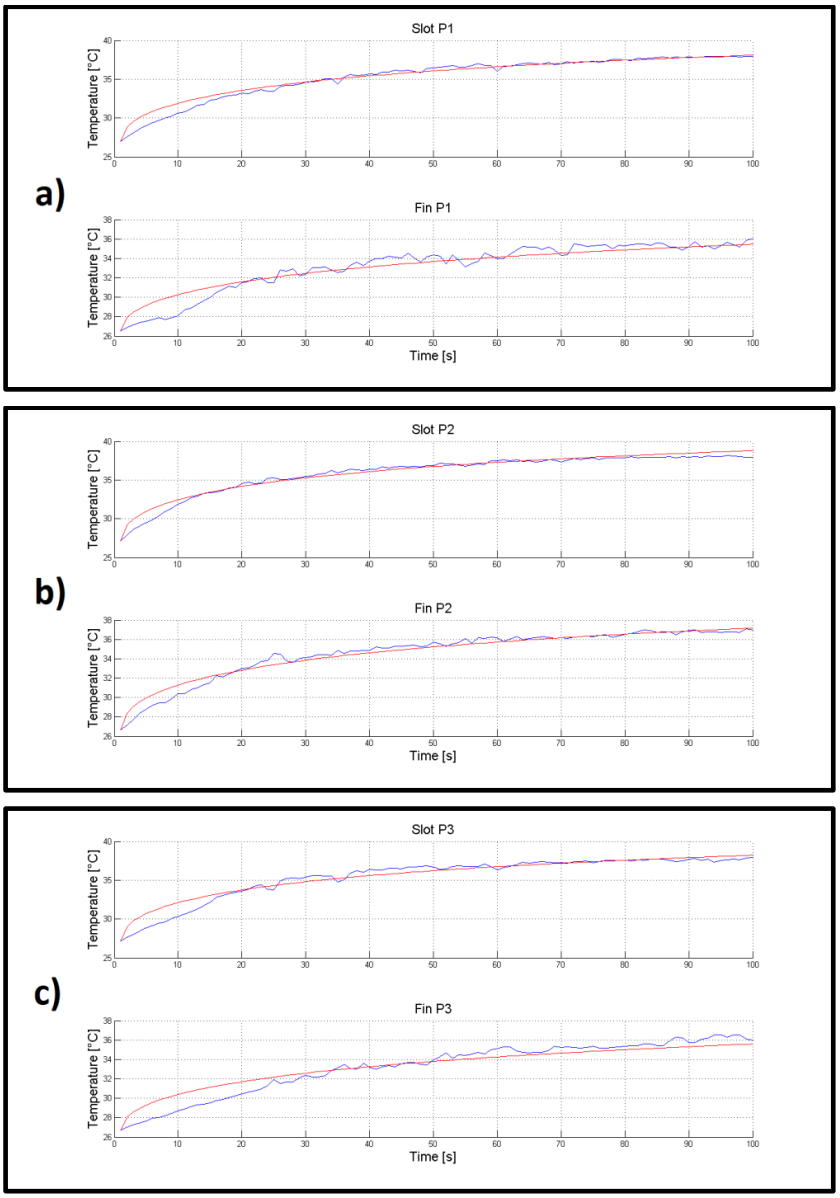

Figure 5.23 : Comparison between the experimental data and numerical for MFR 2 .

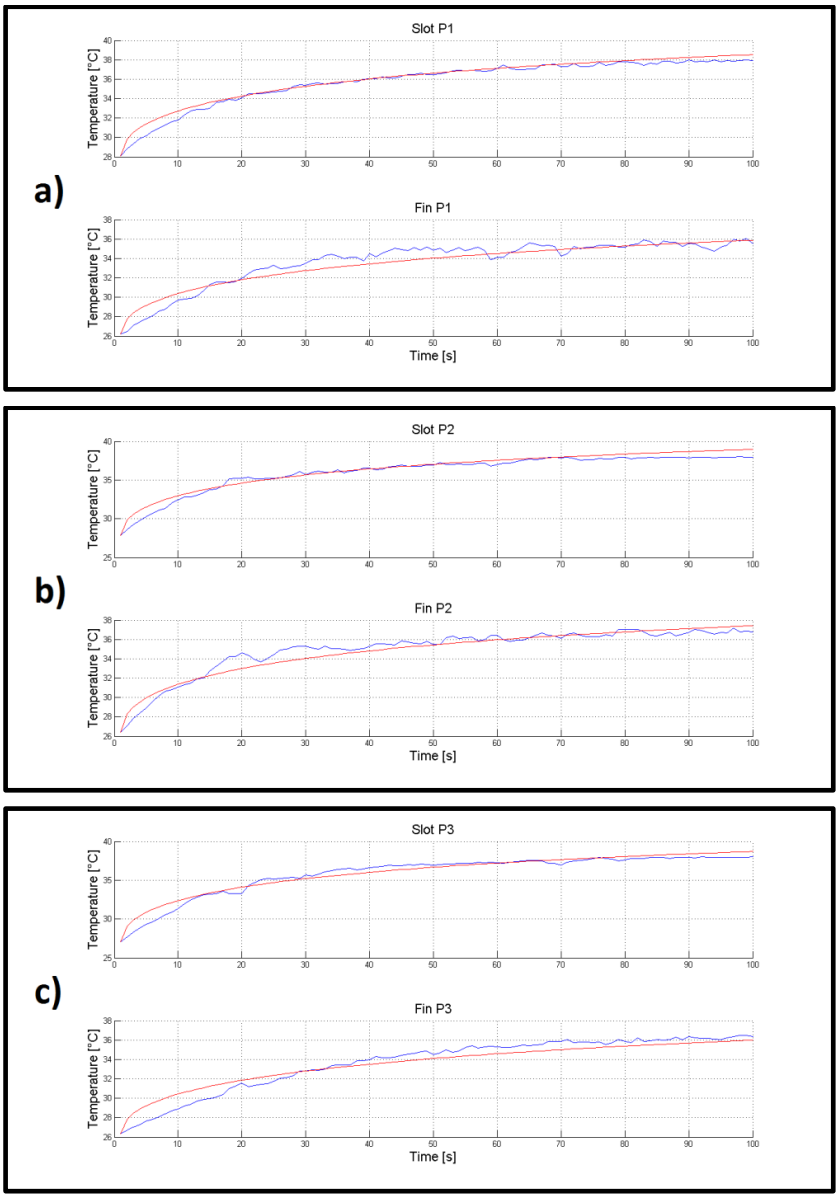

Figure 5.24 : Comparison between the experimental data and numerical for MFR 2,7 .

It's easy to observe that the points in the middle of the cutback (upper curves) fit better with the numerical data than the fin's one. Moreover, for each pixel the *Mean Error* over the entire time interval has been determined, defined as:

$$Mean\ Error = \frac{|T_{Exp} - T_{Num}|}{Time} \tag{5.2}$$

Here are presented the mean error maps (fig. 5.25-26). It is possible to observe that it remains quite low, except for the ribs areas.

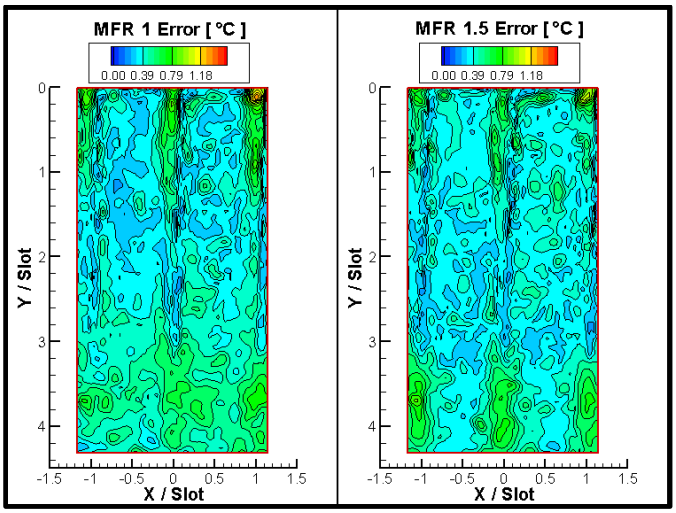

Figure 5.25 : Mean error for MFR 1 and 1,5 .

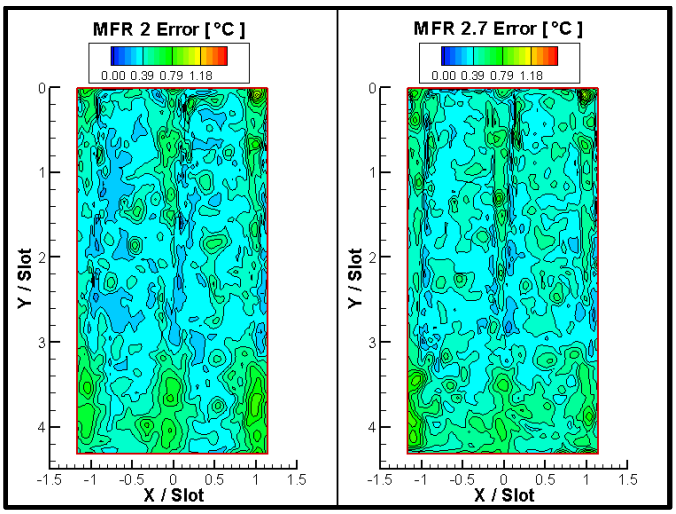

Figure 5.26 : Mean error for MFR 2 and 2,7 .

5.6 Closure

It is important to say that, one of the big issues encountered making these tests, is the right positioning of the lamps to light the pressure side and hence the cutback. Indeed , lamps have been positioned outside the wind tunnel, to avoid that their presence could modify the flow. Moreover, due to the reduced space to attach them and the presence of the other vanes, it has been necessary to accept the fact that shadows are inevitable, especially close to the ribs, in particular close to the ribs, in the high- left part of both the slots studied. That shadow can be observed in all *h*, T_{aw} and *Effectiveness* maps.

Mean error maps in Figures 5.25-26 show that the best fits are obtained in the slot region instead the ribs zones. This is due to the fact that the least square method proposed is a mono-dimensional analysis that does not consider the lateral rib's surfaces. Hence the convective coefficient will be affected by error, as showed in figures 5.25-26. At least it is important to say that the noise present in the right slot for *MFR 2,7* is probably due to the *TLC* thermal degradation, that had as effect the incorrect temperature acquisition.

In figure 5.27 the lateral averaged *convective heat transfer coefficient* are reported, varying the *MFR*.

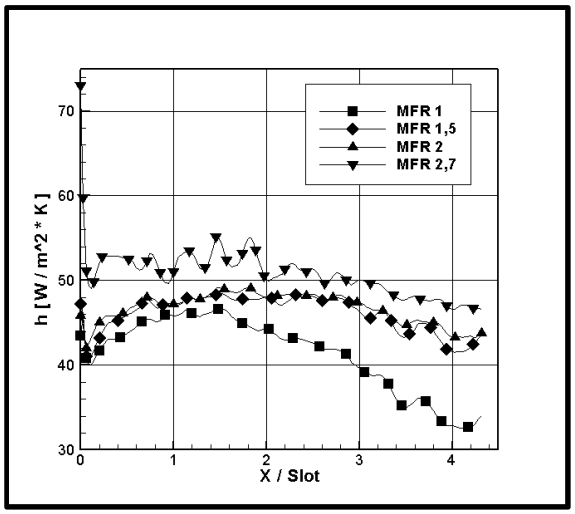

Figure 5.27 : Convective coefficient lateral averaged curves .

It's easy to note that increasing the mass flow injected, the convective coefficient increases too. Moreover note that after X / Slot = 3, *h* has a decreasing behavior, especially for the lower *MFR*.

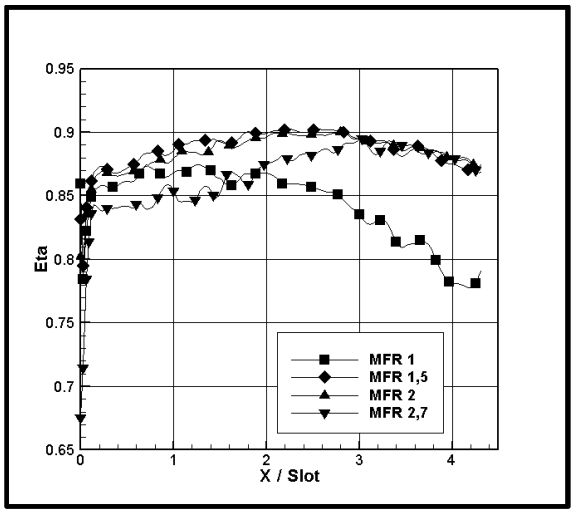

Figure 5.28 : Cooling effectiveness lateral averaged .

Same behavior described before for the *MFR* 1, is showed in figure 5.28, where the lateral averaged *film cooling effectiveness* is presented: generally speaking its value tends to increase with the mass flow injected, remaining high for most of the cutback surface. Based on these observations, the *Mean Error* on lateral averaged data have been calculated and reported in Fig. 5.29. The trend is similar for all the coolant mass flow, till the X / Slot = 2.5 position, except for the lower value again. Indeed, Mean error for that value begins to increase, as the other cases do after X / Slot = 3. In general this behavior is due to the progressive reduction of the vane thickness, close to the trailing edge.

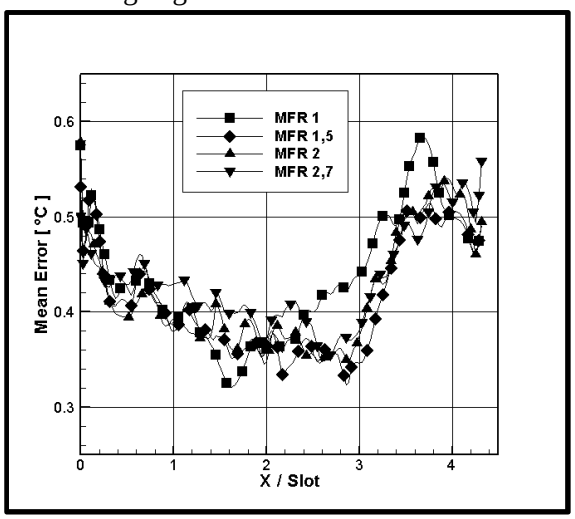

Figure 5.29 : Mean error lateral averaged .

Indeed, as written in chapter 4, the transient technique is a one-dimensional approach to the problem, based on a mathematical problem that has a boundary condition that imposes the body temperature far from the heat transfer surface must be equal to the beginning one. For this reason close to the trailing edge, where the blade thickness is about 2 mm, the heat flux through the suction side is no more negligible.

At this point it is necessary to implement an alternative method to confirm how observed in this test section. For this reason it has been chosen to simplify the physical problem by using a flat plate wind tunnel, in order to have the possibility to test the least square method applied to a known problem and to develop alternative measurement techniques that are expected to solve some of the problems encountered, the biggest one being conduction.

Chapter 6

Flat Plate facility and measurement techniques

6.1 Introduction

Based on the theoretical and experimental approach exposed in the precedent chapters, experiments have been conceived to measure both the film cooling effectiveness and the heat transfer coefficient on a film cooled surface. The case investigated in this section is the *Flat Plate Problem* because it is a simple injection geometry, indeed about flat plate film cooling there are many data available from the literature, and it's easier to clarify what kind of results are expected and thus to validate the measurement techniques and the data processing. In the present chapter the experimental facility and the optical measurement techniques used to acquire data will be described.

6.2 Wind Tunnel

The Flat Plate wind tunnel used in the University of Bergamo laboratory is an open circuit facility too. It is a low speed, continuous running, suction type wind tunnel (fig. 6.1), Plexiglas made to assure optical access everywhere. The air is driven inside of the tunnel through an accelerating inlet section, by a centrifugal fan. The tests have been carried out for a main flow mass flow equal to 0.77 kg/s, assuring a mainstream constant velocity of about 20 m/s.

Overall tunnel operating conditions are continuously monitored: the air velocity is measured by means of a Pitot probe and sidewall pressure taps, while a T-type thermocouple gives the air temperature.

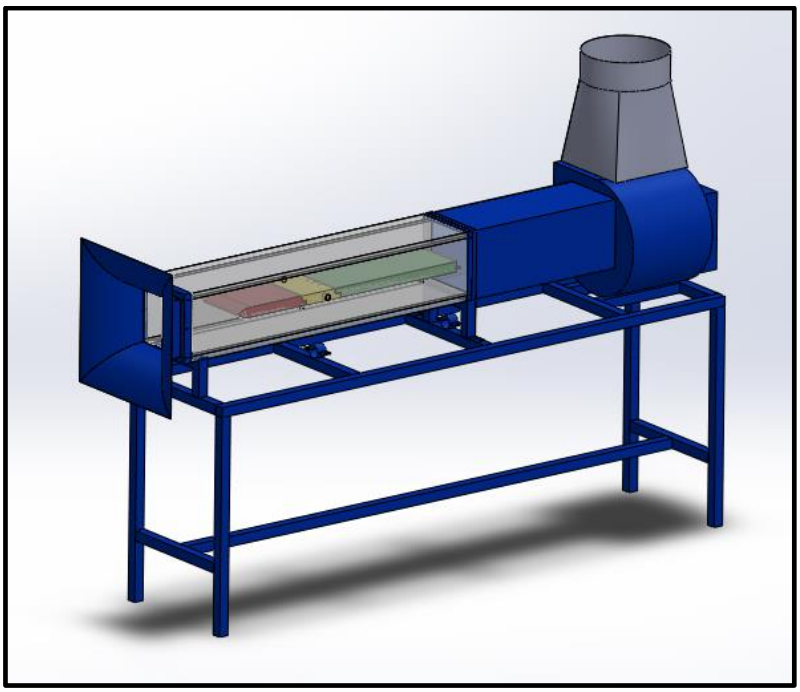

Figure 6.1 : Flat Plate wind tunnel .

6.2.1 Test section

A rendering of the test section is shown in figure 6.2: walls are made in transparent Plexiglas® of 20 mm thickness that allows to perform optical flow measurement and check the aerodynamic probe movement. The tunnel cross section is 0.2 x 0.2 m^2, and it is 1.6 m long.

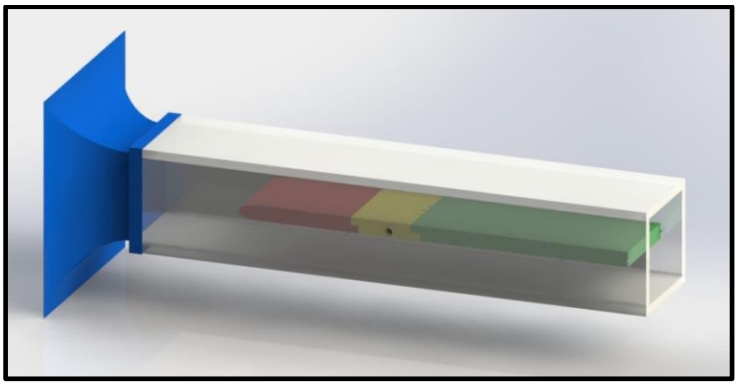

Figure 6.2 : Test section, is possible to recognize the convergent inlet duct (blue) .

A Plexiglas flat plate, 35 mm thick and 0.905 m long, installed in the center of the tunnel provides the film cooled test surface (fig. 6.3). Its nose has a smooth profile, allowing a regular boundary layer development along both flat plate surfaces. Cooling is assured by the presence of a row of three holes (5 mm diameter) located 0.4 m downstream of the flat plate nose. The choice of Plexiglas® has been motivated by its low thermal conductivity (0.19 W/m*K) allowing, in most of the investigated area, to comply with wall adiabatic condition. A modular manufacturing of the flat plate allows easily changing the cooling geometry. This flat plate is composed by three pieces:

1. **Leading edge :** it's a plate which has one side shaped in order to give the possibility to the flux to create gradual boundary layer that will grow for all the plate length;
2. **Injection geometry plate :** is the central part of the plate are made the injection holes and the secondary flow input circuit.
3. **Trailing edge :** is situated downstream the injection holes, that's the portion where will be performed all the optical and aerodynamic tests.

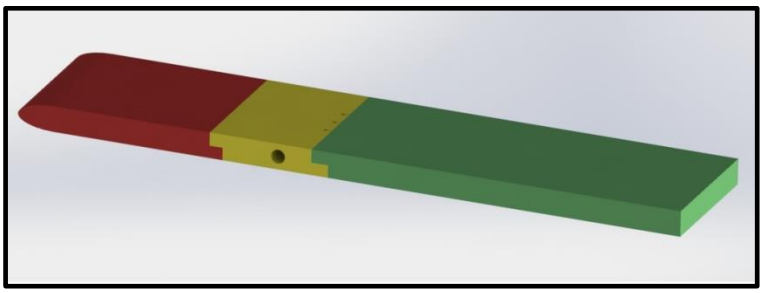

Figure 6.3 : Flat plate: Leading edge (red) , Injection geometry plate (yellow) and trailing edge (green) .

6.2.2 Secondary flow circuit

Cooling is assured by the presence of a row of three holes (5 mm diameter) located 0.4 m downstream of the flat plate nose. Injection holes are fed by a cylindrical channel (20 mm diameter) manufactured inside of the flat plate thickness. The secondary air is supplied from both sides of the channel. This internal channel will perform as a plenum for the cooling holes, as its diameter is sufficiently large compared with the hole one. The coolant flow is provided by the air shop circuit. The injected mass flow is measured by a flow meter (200 nl/min full scale) (fig 6.4), while coolant pressure and temperature are measured inside of the supply channel by means of pressure taps and T-type thermocouples. The maximum estimated uncertainty on the coolant mass flow was ± 5% at the lowest injection condition.

6.2.3 Secondary Flux Heater

The injected air is heated while the main flow is at room temperature. The heater is a rectangular sheet of 75 x 1015 x 1.4 mm, including an electric resistance insulated with Teflon and neoprene (fig.6.4) and wrapped around the 20 mm diameter pipe.

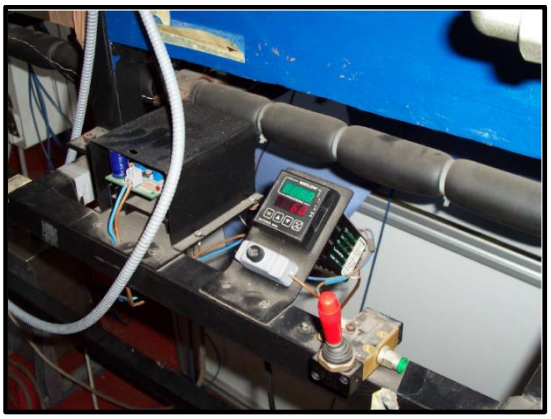

Figure 6.4 : secondary flow pipe with insulated heater and regulation system.

An automatic control system allows maintaining the set point with an accuracy of ± 0.1%, and a stability of ± 0.2°C.

6.3 Pressure Sensitive Paints

6.3.1 Introduction to PSP [6.1]

This is a relatively new technique for pressure fields measurement on surfaces. Paints are composed by a polymeric matrix where are mixed luminescent molecules (fig. 5.11).

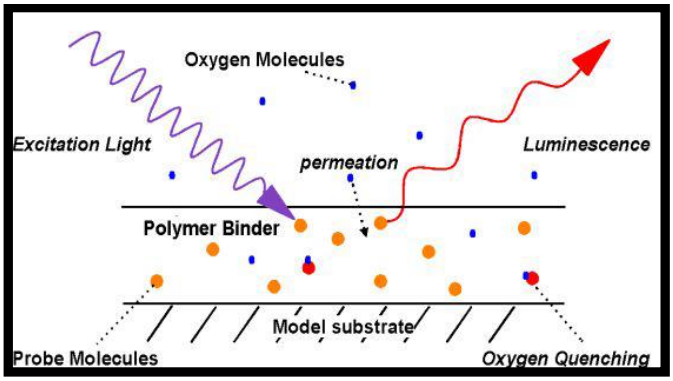

Figure 5.11 : Pressure Sensitive Paint functioning .

These paints, absorb oxygen from air proportionally with the pressure, modifying the color *Intensity*. Once excited with appropriate lights, the coating will emit a radiation inversely proportional to the quantity of oxygen absorbed. Hence, higher pressures, give low *intensity* and vice-versa. The acquiring method is similar to the TLC one, the main difference stays in the choice of the parameter after the conversion to HSI.
The oxygen quenching mode can be described mathematically, by using the *Stern-Volmer* formula:

$$\frac{I_{Max}}{I} = 1 + Kc \tag{5.1}$$

$$c = S \cdot X \cdot p \tag{5.2}$$

Where:

- I_{max} : Maximum intensity emitted in oxygen absence (void condition);
- S : Temperature dependent coefficient;
- X : oxygen mole fraction in air;
- p : Surface pressure.

Since during laboratory experiments *K,S* and *X* remains constant, it will be possible collapse all these coefficients in non-dimensional groups, in order to obtain a temperature function alone (5.3).

$$\frac{I_0}{I} = A(T) + B(T)\frac{p}{p_0} \tag{5.3}$$

Function that is the *PSP Calibration Curve,* which relate local Intensity uniquely with local pressure, parameterized with the temperature.

6.3.2 PSP Calibration [6.2]

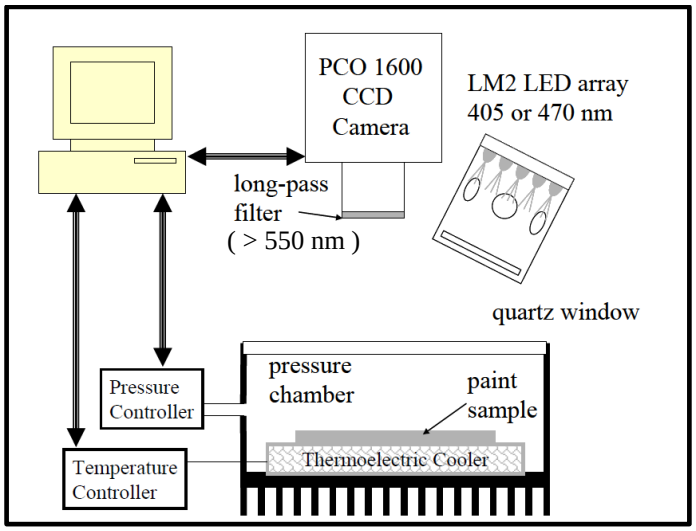

Figure 5.12 : PSP Calibration System .

In figure 5.12 is showed a complete scheme of a calibration system. This procedure needs of a *calibration chamber*, which is a box with one transparent side, able to hold the void. In this chamber, moreover, is situated a Peltiér module and a pressure outlet, the first to ensure a constant surface temperature during the calibration, the second to monitor the internal pressure. PSP are lighted with LED lamp, having an emission wavelength of 400 nm (UV light), as prescribed from the paint factory. Images are acquired, using a high pass filter, having threshold at 550 nm, which is the paint emission low limit. At the beginning of each calibration or test, it is necessary to acquire a dark image, a picture made in dark ambient with led lamp turned off. this is to measure the camera sensor's noise, and hence remove it from data. Repeating the calibration procedure for more paint temperature, the calibration

curve obtained will have a linear or a parabolic shape, depends from the kind of PSP used (fig. 5.13):

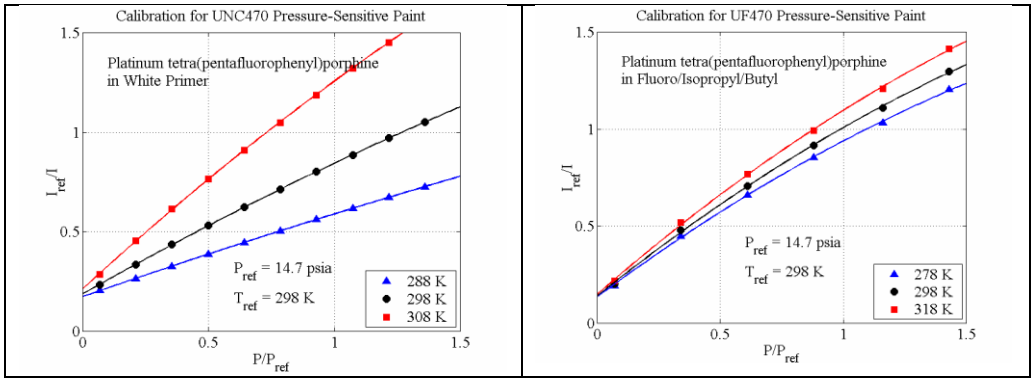

Figure 5.13 : Calibration curve of two different type of PSP, linear on the left, and parabolic on the right.

Chapter 7

Experimental Tests and Results

7.1 Introduction

In this section the experimental methodology will be described and the results obtained with the *Least Square Method* applied to a flat plate film cooling problem will be discussed. Two different scaled-up injection geometries has been tested: *cylindrical holes* and *Fan Shaped holes (Gritsch configuration).* The increased cross-sectional area at the hole exit, compared to the cylindrical one, leads to a reduction of the mean velocity and, thus, of the momentum flux of the jet exiting the hole. Therefore, the penetration of the jet into the mainflow is reduced, resulting in an increased cooling efficiency [7.1]. Moreover, the larger lateral extension of the hole exit section results in a high lateral spreading.

The goal of these tests is to better understand the least square method behavior, comparing the obtained results with the literature and between the different measurement techniques used, also in order to better understand the results presented in chapter 5.

7.2 Experimental Methodology

As previously described, the transient technique involves the study of the superficial thermal history after a step variation of the flow temperature.

7.2.1 Injection geometries

A cylindrical hole geometry has been tested first (fig. 7.1), whose geometrical characteristics are described in tab. 7.1.

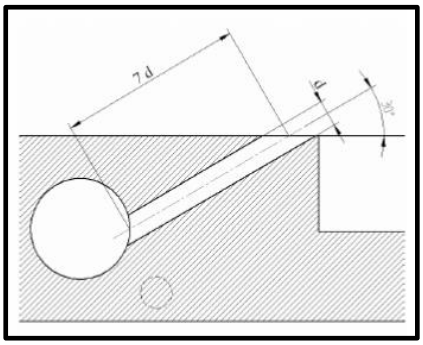

Tab. 7.1 : Cylindrical Holes geometry	
Diameter	**5 (mm)**
L/D	**10.7**
Pitch angle α	**30°**

Figure 7.1 : Cylindrical holes section and geometric characteristics.

The second geometry tested in this session was the *Gritsch Fan Shaped hole* (fig. 7.2) whose geometric characteristic are reported in Tab. 7.2.

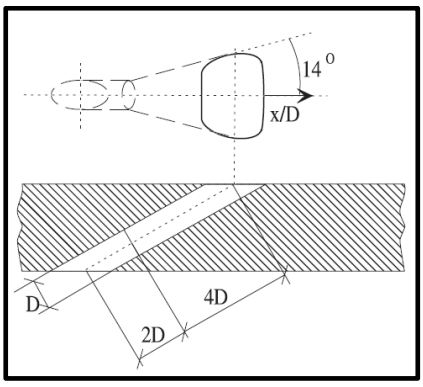

Tab. 7.1 : Fan Shaped Holes geometry	
Diameter	**5 (mm)**
L/D	**6**
Pitch angle α	**30°**

Figure 7.2 : Fan shaped holes section and geometric characteristics.

7.2.2 Test Conditions

Mainflow conditions are reported in tab. 7.3 :

Tab. 7.3 : mainflow condition	
$\mathbf{U_\infty}$	**20 (m/s)**
$\mathbf{Re_\infty}$	**$1.1\ 10^5$**
$\mathbf{Tu_\infty}$	**0.5 %**
δ*/D	**0.09**
$\mathbf{H_{12}}$	**1.35**
DR	**0.95**

Injection conditions have been varied between BR 0.3, 0.5 and 1 for cylindrical holes, and BR 0.5,1,1.5 and 2 for fan shaped tests. The reason of this choice is the capability of the second geometry to maintain a good superficial coverage for high blowing rate (1.5 and 2), while the simple cylindrical holes show lift off for BR=1 yet. Being the goal of the present section to check the least square method, it has been retained enough to inject at these conditions.

7.3 Results

7.3.1 Cylindrical Holes

In figure 7.3 are presented the adiabatic effectiveness obtained during this test session, calculated by using equation (5.1). In figure 7.4 are presented the adiabatic effectiveness obtained by Barigozzi-Franchini-Perdichizzi [7.2]. As expected, cylindrical geometry shows an acceptable persistence on the cooled surface for low *blowing ratio's* values.

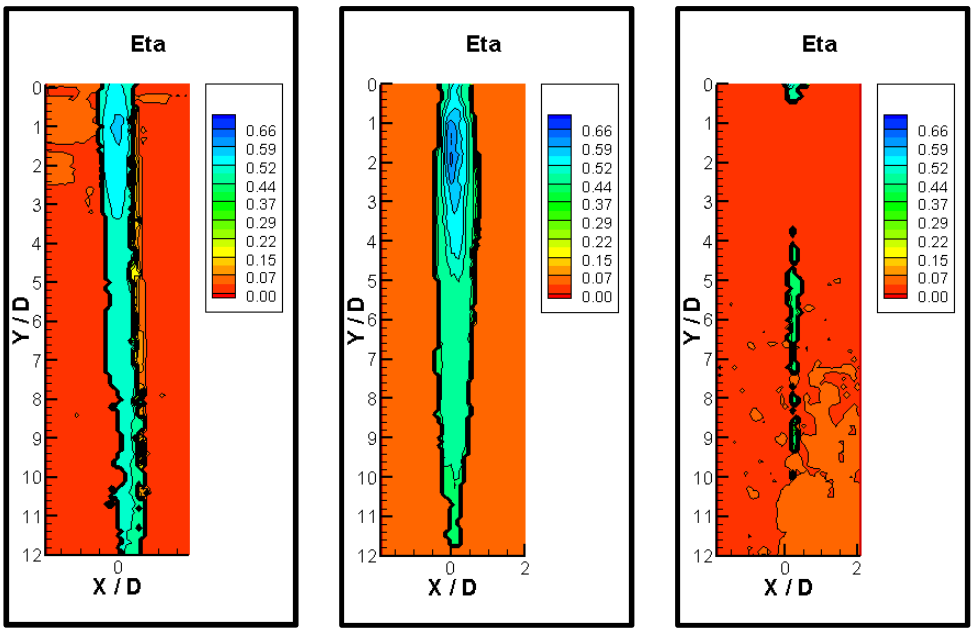

a) *b)* *c)*

Figure 7.3 : Cylindrical holes cooling effectiveness: a) BR=0.3, b) BR=0.5,c) BR=1.

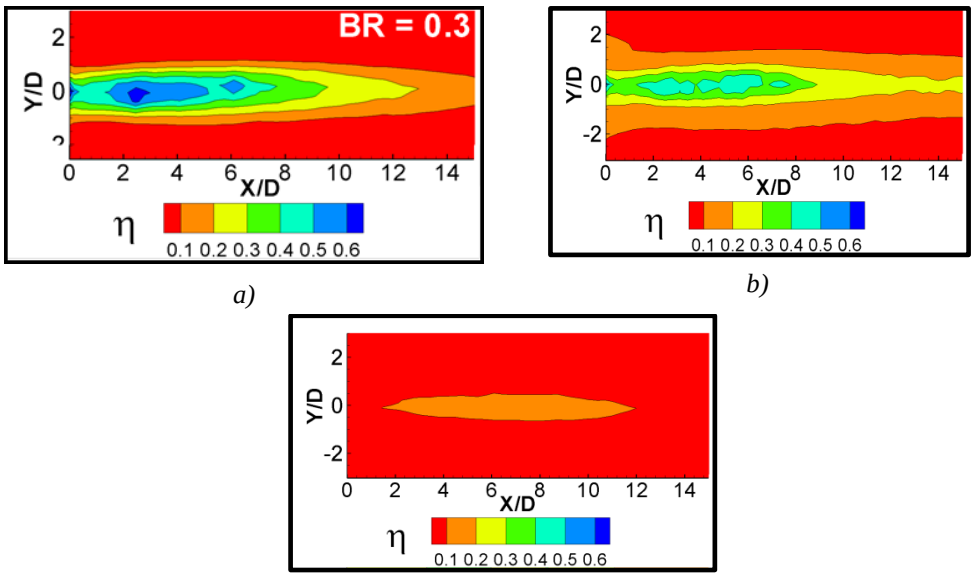

a) *b)*

Figure 7.4 : Cylindrical Holes Adiabatic Effectiveness [7.2]: a) BR=0.3, b) BR=0.5,c) BR=1.

It is possible to observe that the effectiveness values are close with the literature ones, in particular, it has been detected the same behavior for *BR = 1*, indeed the cooling jet separates and reattaches almost at the same position. It is possible to compare the results obtained in the University of Bergamo Flat Plate Tunnel, with the results obtained at Virginia Tech flat plate facility, by using PSP technique (fig. 7.5):

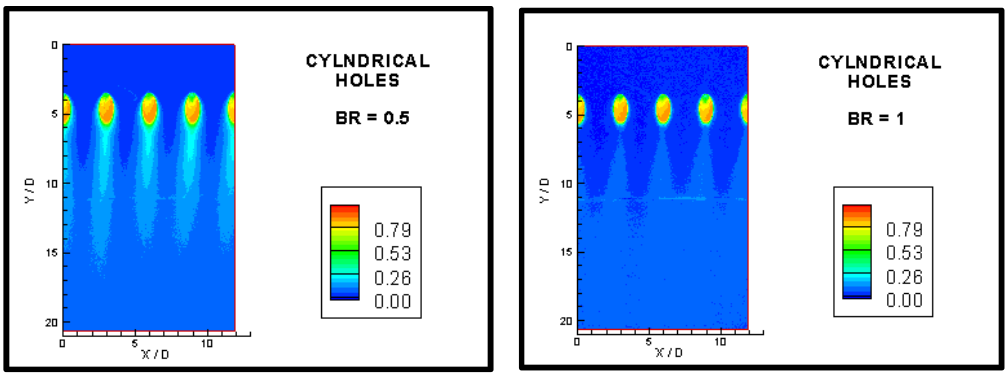

b) *c)*

Figure 7.5 : Pressure Sensitive Paint adiabatic effectiveness.

It's easy to see that the jet persistency on the surface is almost the same for both precedents figures (for BR=0.5). Moreover this map shows other details, especially for low effectiveness points that are impossible to detect with thermal techniques. The advantage of this measurement system, indeed, is the complete absence of heat transfer, avoiding all the thermal conduction problems that usually are to be considered for other measurement methods. In second instance, it is important to note that for higher BR, the coolant vein separates almost completely from the surface, to reattach, and hence increase the adiabatic effectiveness, after 2-4 diameters from the exit, as seen in thermal tests, giving the same lower resolution than this last approach (fig. 7.6).

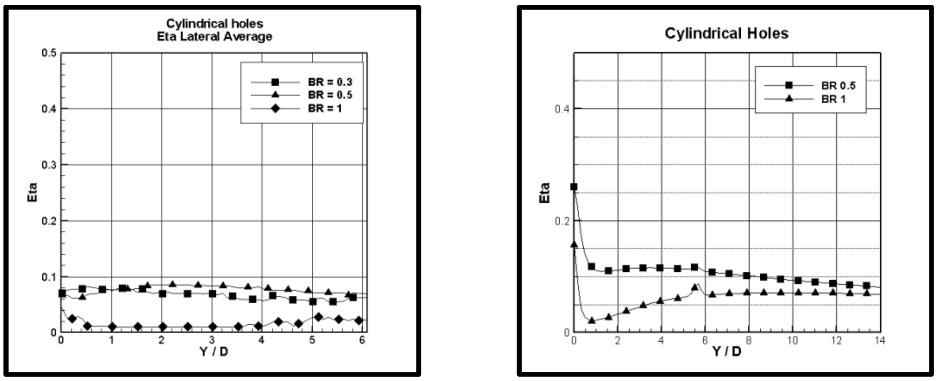

Figure 7.6 : Adiabatic Effectiveness Lateral Average, Least square method (left) and PSP method (right).

At least, the calculated heat transfer coefficients have been compared with the literature [7.3-5] and a good agreement with these data was seen, as showed in figure 7.7-8.

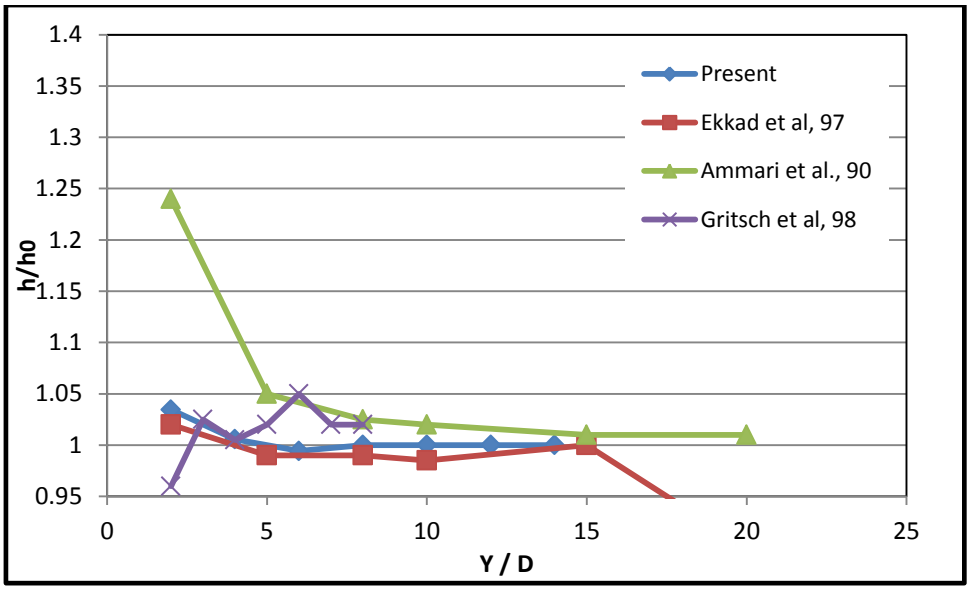

Figure 7.7 : BR = 0.3, h/h_0 confront.

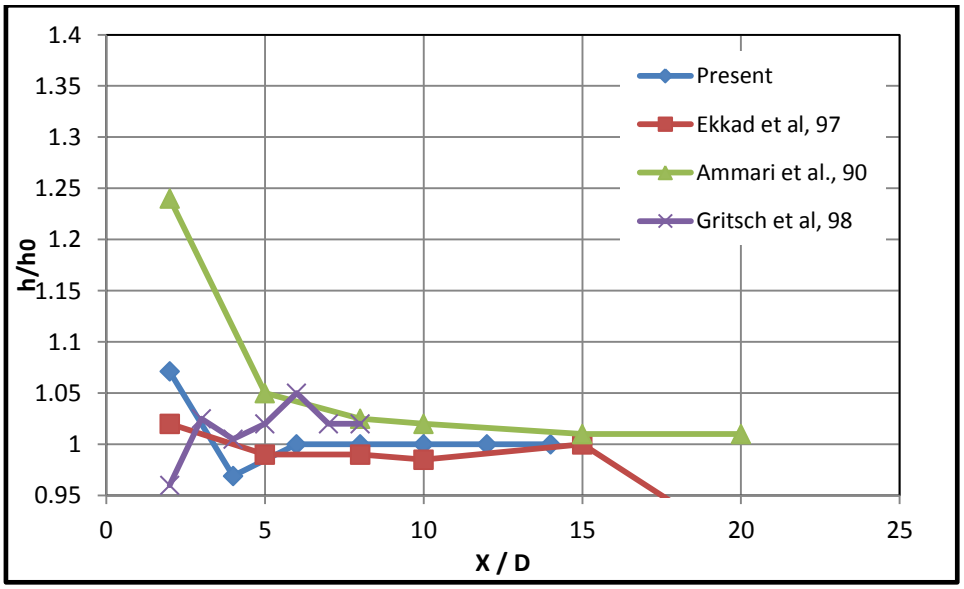

Figure 7.8 : BR=0.5 , h/h_0 confront.

7.3.2 Fan Shaped Holes

Fan Shaped geometry effectiveness is shown below (fig. 7.9):

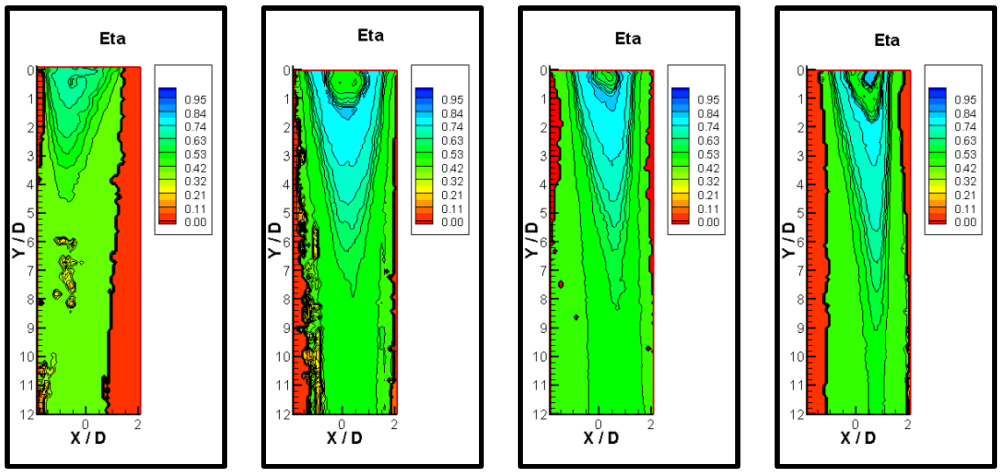

a) *b)* *c)* *d)*

Figure 7.9 : Fan Shaped Holes Cooling effectiveness: a) BR=0.5 ; b) BR=1 ; c) BR=1.5; d) BR=2.

And their lateral averaged values are presented in figure 7.10:

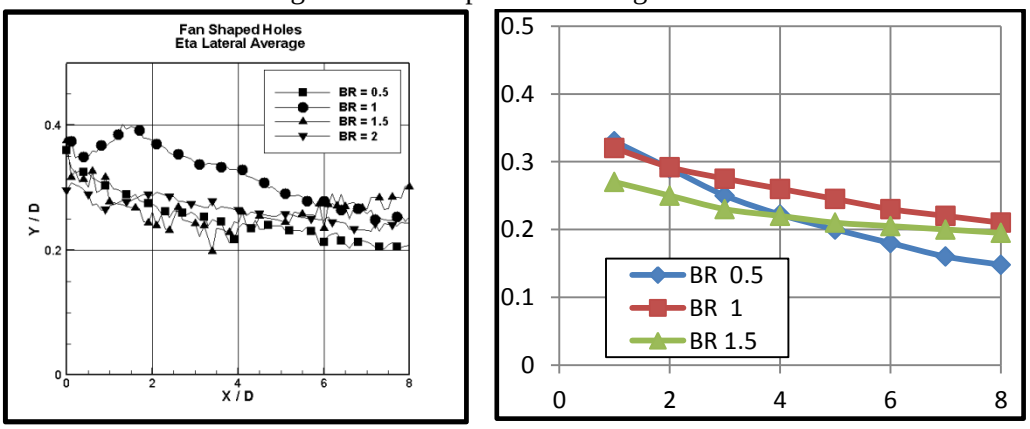

Figure 7.10 : Fan Shaped Cooling effectiveness lateral average.

These results, compared with the lateral averaged effectiveness found by Gritsch [7.1], show the same trend up to 8 diameter downstream, but the values scale is

slightly higher. This could be due to a different lateral extension in the averaging process.
Some convective coefficient maps are proposed in figure 7.11 and their lateral average in figure 7.12.

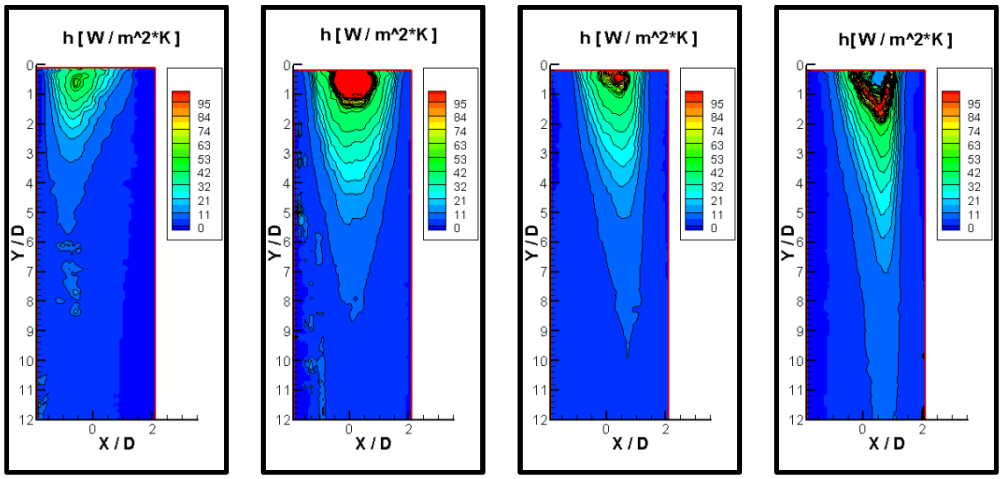

Figure 7.12 : Fan Shaped Holes Heat Transfer Coefficient : a) BR=0.5 ; b) BR=1 ; c) BR=1.5 ; d) BR = 2 .

From maps 7.9 and 7.12 the typical behavior of this injection geometry is confirmed: most of the coolant is located in the central part of the jet, and hence there is a higher lateral spreading of effectiveness and an increase of the central "high efficiency region" length as well, due to the injected mass flow increase. Moreover, right to the hole exit, a small separation zone is present, and it's detected by an effectiveness local decrease.

7.4 Closure

Results presented in this chapter show a good consistency, in terms of effectiveness, with other works about the same problem. A typical error between experimental and numerical temperature histories is shown in figure 7.13.

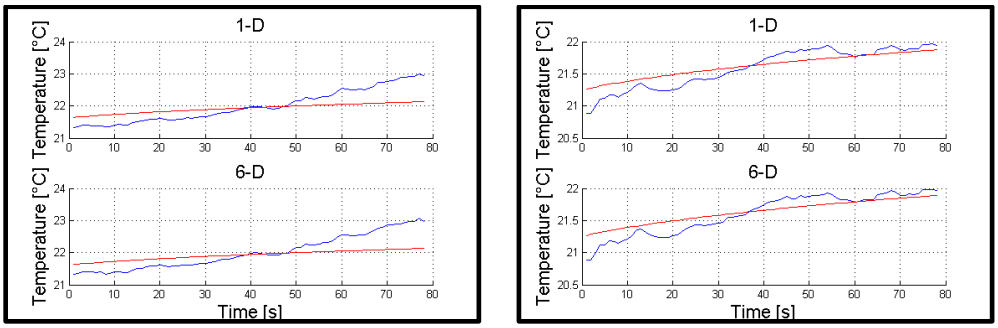

Fan Shaped BR = 1.5 ***Fan Shaped BR = 2***

Figure 7.13 : Comparison between experimental temperature *(Blue)* and numerical temperature *(red)* .

It's easy to observe that temperature history is reasonably well captured, even if some differences do exist, mostly because the signals are affected by noise. An example of *Mean error* map is presented in figure 7.14.

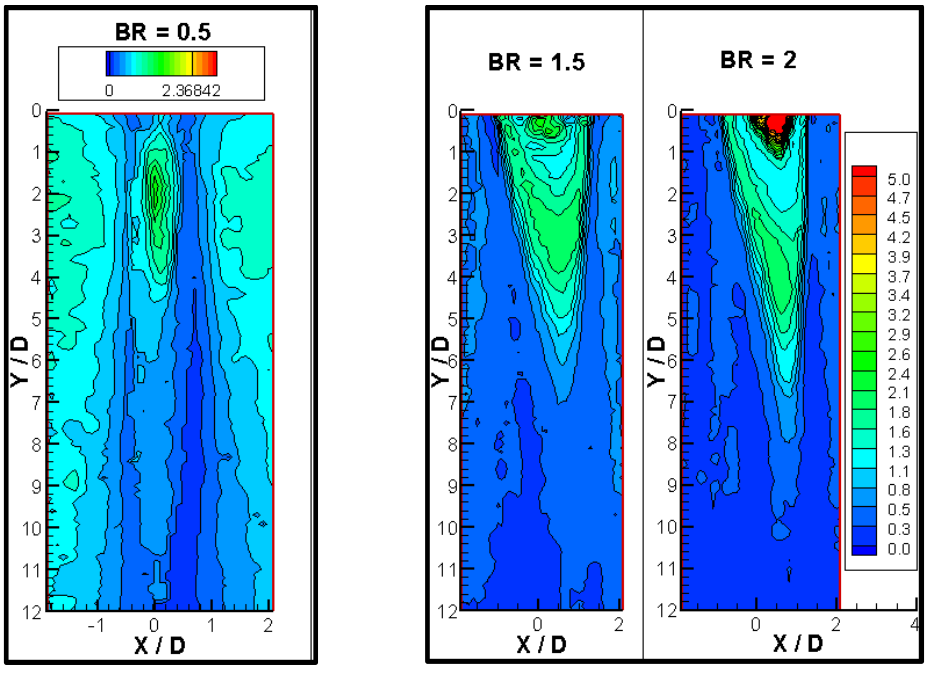

Figure 7.14 : Cylindrical Holes Mean Error: a) cylindrical and b) and c) fan shaped

Despite the linear vane cascade case, where the mean error over the whole surface was less than 0.7°C, in this case, maps show that the error is greater than 1.5-2°C quite everywhere and this can also be related to the different test time duration. Anyway, it is interesting to note the regions where errors are bigger, i.e. where effectiveness as well as heat transfer coefficient values are higher (in the core of the jet).

Chapter 8

Closure

8.1 Conclusions

The investigation reported in this Thesis can be divided into two parts: the first one is devoted to the aero-thermal analysis of a nozzle vane cascade with pressure side cooling through holes and a cutback trailing edge. A full characterization of the aerodynamic mixing process between coolant and mainstream was carried out by means of boundary layer traverses performed along the vane pressure side for different injection condition and downstream Mach number. These data showed the presence of an uneven sharing between injection rows. This in turn resulted in increased turbulence characteristics. Reduced turbulence levels were instead observed downstream of row #2. In any case, a certain degree of anisotropy characterizes the turbulence characteristics. Rising the mainstream Mach number increases the flow acceleration along the pressure side keeping the jets closer to the wall and reducing turbulence. The thermal

investigation, focused on the cutback region, enlightened several problems related to the application of the transient liquid crystal technique (TLC) to a complex geometry. The second part of this thesis is thus devoted to deepen and validate heat transfer coefficient and film cooling effectiveness transient measurement technique, also trying to identify alternative solutions. In this context, a flat plate geometry was tested, as it is a well-documented flow condition with many data available from the literature. In particular, two cooling hole geometries were selected and tested: a cylindrical hole configuration and a fan-shaped solution. Wide banded TLC and pressure sensitive paints (PSP) were selected as measurement techniques. In the first case, the technique is new, but it should be improved to get more accurate results; for the second one, it is a new technique that was necessary to develop at Bergamo University. Results from transient TLC technique were in reasonable agreement with literature data, even if some problem related to noisy signals and to conduction effects still exist.

To improve the consistency with the physical problems, it will be necessary to better refine the post processing method and help it by using, coupled with the traditional thermal methods, another experimental measurement technique, as the Pressure Sensitive paints, in order to have the possibility to perform test that are completely adiabatic, and hence to correct optimized results.

Indeed, as observed comparing the Mean Error maps, bigger error are found in those regions characterized by slow and little thermal variation in time. The main difference between the linear vane cascade and flat plate tests stays in the temperature difference between the final and the starting point. For the first data set, it is about 4-5 °C , while for the second it stays quite everywhere below the 2°C. This could mean that the most important part of the superficial thermal history is situated in the first 10-20 seconds after the injection, and this portion is the one that rule the Adiabatic wall temperature and the convective coefficient, so the optimization method should be improved in order to be more sensitive, and applied to shorter time interval. Moreover, the experimental method accuracy must be improved too, in order to reduce the data noise.

The next step of this research is represented by a new set of tests, by using the Pressure Sensitive Paints for each geometry tested, in order to extract the Adiabatic temperature coupling its results with the transient technique method, thus forcing the solution to more correct data. The power of this new measurement technique stays in the complete absence of heat transfer, so the problems due to the thermal conduction are completely avoided. Moreover it could have a great spatial resolution, depending only on the optical acquiring system, giving extremely precise results.

Bibliography

[1.1] A. Perdichizzi : *"Turbine a gas"* , dispense del corso di Sistemi energetici 2005/06, pag. 2-4 , 40-47;

[1.2] R. J. Goldstein, *"Film cooling"* ???

[1.3] C. Carcasci, B. Facchini, L. Innocenti : *"Heat Transfer and Pressure Drop Evaluation in Thin Wedge Shaped Trailing Edge"*, ASME Paper GT-2003-38197, 2003.

[1.4] P. Martini, A. Schulz, C.F. Whitney, E. Lutum : *"Experimental and Numerical Investigation of Trailing Edge Film Cooling downstream of a Slot with Internal Rib Arrays"*, Proceeding of the 5th European Conference on Turbomachinery Fluid Dynamics and Thermodynamics (ETC5), pp. 487-500, 2003.

[1.5] P. Martini, A. Schulz, S. Wittig : *"Experimental and Numerical Investigation of Trailing Edge Film Cooling by Circular Coolant Wall Jets Ejected from a Slot with Internal Rib Arrays"*, ASME Paper GT-2003-38157, 2003.

[1.6] O. Uzol, C. Camci, B. Glezer : *"Aerodynamic Loss Characteristics of a Turbine Blade with Trailing Edge Coolant Ejection: Part 1- Effect of Cut-Back Length, Spanwise Rib Spacing, Free-Stream Reynolds Number, and Chordwise Rib Length on Discharge Coefficients"*, J. of Turbomachinery, vol. 123, pp. 238-248, 2001.

[1.7] O. Uzol, C. Camci : *"Aerodynamic Loss Characteristics of a Turbine Blade with Trailing Edge Coolant Ejection: Part 2- External Aerodynamics, Total Pressure Losses, and Predictions"*, J. of Turbomachinery, vol. 123, 249-257, 2001.

[1.8] P. Martini, A. Schulz, C. F. Whitney, E. Lutum : *"Experimental and Numerical Investigation of Trailing edge Film Cooling Downstream of a Slot with Internal Rib Arrays"*, Proc. Inst. Mech. Eng., Part A, vol. 217, pp. 393-401, 2003.

[1.9] P. Martini, A. Schulz, H.-J. Bauer : *"Film Cooling Effectiveness and Heat Transfer on the Trailing Edge Cut-back of Gas Turbine Airfoils with Various Internal Cooling Designs"*, Proc. ASME Turbo Expo 2005, GT2005-68083.

[1.10] F. E. Ames, J. D. Johnson, N. J. Fiala : *"Gill Slot Trailing Edge Aerodynamics - Effects of Blowing Rate, Reynolds Number and External Turbulence on Aerodynamics Losses and Pressure Distribution"*, Proc. ASME Turbo Expo 2007, GT2007-27399.

[1.11] H. J. Rehder : *"Investigation of Trailing Edge Cooling Concepts in a high Pressure Turbine Cascade – Aerodynamic Experiments and Loss Analysis"*, Proc. ASME Turbo Expo 2009, GT2009-59303.

[1.12] Dannhauer A. 2009 : *"Investigation of Trailing Edge Cooling Concepts in a High Pressure Turbine Cascade – Analysis of the Adiabatic Film Cooling Effectiveness"*, ASME Paper GT2009-59343.

[3.1] P. Puddu, F. Cambuli, M. Paderi, M. Ghiani *"Measurements and numerical simulations in a gas turbine cascade with cutback blade trailing edge"*
Proceedings of the 10th International Symposium on Experimental and Computational Aerothermodynamics of Internal Flows, Brussels, 2011

[3.2] Pietrzyk J.R., Bogard D.G., Crawford, M.E. (1989) *Hydrodynamics Measurements of Jets in Crossflow for Gas Turbine Film Cooling Application*, ASME J Turbomachinery, 111, 139-145.

[4.1] R.J. Vedula , D.E. Metzger : *"A Method for the Simultaneous Determination of Local Effectiveness and Heat Transfer Distributions in Three-Temperature Convection Situations"* , International Turbine and Aeroengine Congress and exposition, 1991;

[4.2] S. Rainieri, G. Pagliarini : *"Data Filtering applied to Infrared Thermographic measurements intended for the estimation of Local Heat Transfer Coefficient"* , Experimental Thermal and Fluid Science 26 (2002) 109-114 .

[6.1] E. L. Yuksek , C. P. Britcher *"Pressure Sensitive Paint: practical application in wind tunnel"*.

[6.2] Innovative Scientific Solutions, Inc. *"Binary Pressure Sensitive Paint".*

[7.1] M.Gristch , A. Shulz , S. Wittig *"Adiabatic wall effectiveness measurements of film-cooling holes with expanded exits".* ASME Paper 97-GT-164.

[7.2] G. Barigozzi , G. Franchini , A. Perdichizzi *"The effect of an upstream ramp on a cylindrical and fan shaped hole film cooling – part II: Adiabatic Effectiveness results".*

[7.3] Gritsch, M., Schulz, A., Wittig, S., 1998, *"Heat Transfer Coefficient Measurements of Film-Cooling Holes with Expanded Exits"*, ASME Paper 98-GT-28.

[7.4] Ammari H.D., Hay N., Lampard D., 1990, *"The effect of density ratio on the heat transfer coefficient from film-cooled flat plate"*, ASME Transactions 112, 444-450.

[7.5] Ekkad S.V., Zapata D., Han J.-C., 1995, *"Heat transfer coefficients over a flat surface with air and CO2 injection through compound angle holes using a transient liquid crystal image method"*, ASME Paper 95-GT-10.